


Research Article

Mid- to Late Holocene geomorphodynamics in a long-term settled mountain catchment in the Pergamon micro-region, western Turkey

Xun Yang^{a*} , Fabian Becker^a, Moritz Nykamp^a, Bernhard Ludwig^{a,b}, Mehmet Doğan^c, Turhan Doğan^d, Daniel Knitter^e and Brigitta Schütt^a

^aDepartment of Earth Sciences, Institute of Geographical Sciences, Physical Geography, Freie Universität Berlin, Malteserstraße 74-100, 12249 Berlin, Germany;

^bDeutsches Archäologisches Institut (DAI), Istanbul Department, İnönü Caddesi 10, 34437 Istanbul, Turkey; ^cDepartment of Geography, Faculty of Letters, Ege University, 35100 Bornova-Izmir, Turkey; ^dTübitak National 1 MV AMS Laboratory, Marmara Research Center, Earth and Marine Science Institute, Barış Mahallesi, 1 Dr. Zeki Acar Caddesi, PK 21 41470 Gebze Kocaeli, Turkey and ^eOEKO-LOG Field Research, Joachimsthaler Straße 9, 16247 Parlow, Germany

Abstract

From 300 BC to AD 300, the city of Pergamon underwent a profound transformation that impacted the rural settlement patterns and the concomitant geomorphodynamics. We present a geoarchaeological study in a long-term settled catchment in the Pergamon micro-region to disentangle the Holocene geomorphodynamics and triggering factors, for example, climate change and human activity. The analyses of eight radiocarbon-dated sediment profiles from the Tekkedere alluvial fan and its catchment indicate four principal sedimentation phases. Phase 1 (ca. 6.2 to 5–4 ka) is dominated by the floodplain aggradation of the receiving Bakırçay River, which is followed by the formation of floodplain soils (phase 2). Substantial geomorphodynamic changes occurred around 4 ka (phase 3), when the edge of the floodplain was buried by fan sediments of the tributary Tekkedere creek. This is attributed to supraregional aridization and rapid climate change events, superimposed by the onset of local human activities. Repeated cycles of coarse- and fine-textured fan sediments with age inversions after ca. 3.8 ka and valley infills younger than 1300 yr BP indicate the strong erosion and redeposition of sediments in phase 4. These increased geomorphodynamics may coincide with the changing settlement pattern and thus reflect human–environment interactions.

Keywords: Sediment dynamics, Floodplain–alluvial fan interplay, Settlement pattern, Bakırçay River, Geoarchaeology

(Received 8 April 2022; accepted 19 December 2022)

INTRODUCTION

Holocene environmental changes and the interplay between natural conditions and human activities are intensely discussed research topics (Constante et al., 2010; Bellin et al., 2013; Ackermann et al., 2014) that cover, for example, soil erosion, natural hazards, and settlement location decisions (Black et al., 2011). The complex causes of changing geomorphodynamics in Mediterranean landscapes have been debated for more than 50 years (Vita-Finzi, 1969; Butzer, 2005; Duser et al., 2011; Walsh et al., 2019; Jouffroy-Bapicot et al., 2021). The main issue is the degree to which geomorphological changes are triggered by environmental fluctuations (Avni et al., 2006; Jalut et al., 2009; Roberts et al., 2011), human decisions, and socioeconomic conditions (van Andel et al., 1990; Remondo et al., 2005; Roberts, 2019) or their complex interactions (Brisset et al., 2013; Verstraeten et al., 2017; May et al., 2021). Hence, disentangling these related

factors is not always straightforward (Fuchs, 2007; Walsh et al., 2019). Past human settlement strategies are, conversely, to some extent related to the geomorphic locations and processes (Kondolf and Piégay, 2011; Aucelli et al., 2018). River terraces and piedmonts, for example, are often preferred settlement locations (e.g., Kidder et al., 2008; Knitter, 2013; Lü et al., 2019).

In the eastern Mediterranean, the meta-analyses of Holocene terrestrial sediment archives indicate several phases of increased geomorphodynamics (Duser et al., 2011; Walsh et al., 2019), which especially occur during the periods when human impacts on the environment became more important. This general trend, however, might not be equally seen in all Mediterranean areas due to diverse settlement patterns and landscape sensitivities. A ground check in small valleys occupied by remote settlements and under the background of large urban centers could thus provide advanced and multilayered insights.

A suitable study area for such a ground check is the ancient city of Pergamon and its micro-region. As one of the most important and largest cities in Asia Minor (Pirson, 2017), Pergamon experienced a profound transformation from the Hellenistic Period to the Roman Imperial Period (300 BC–AD 300) (Pirson, 2020). During this time, the urban area of Pergamon doubled (Wulf, 1994) in tandem with a significant increase in population and an intensive public building program (Pirson,

*Corresponding author at: Xun Yang, Department of Earth Sciences, Institute of Geographical Sciences, Physical Geography, Freie Universität Berlin, Malteserstraße 74-100, 12249 Berlin, Germany. E-mail address: xun.yang@fu-berlin.de

Cite this article: Yang X, Becker F, Nykamp M, Ludwig B, Doğan M, Doğan T, Knitter D, Schütt B (2023). Mid- to Late Holocene geomorphodynamics in a long-term settled mountain catchment in the Pergamon micro-region, western Turkey. *Quaternary Research* 114, 69–92. <https://doi.org/10.1017/qua.2022.73>



2020). The population probably reached 180,000 people in the entirety of the Pergamon micro-region (Zimmermann, 2011). The contemporary demilitarization of Pergamon's hinterland increased the importance of rural settlements (Fig. 1), where possibly around 70% of the population lived (Pavúk and Horejs, 2018; Pirson, 2020; Laabs and Knitter, 2021). In this micro-region, diverse archaeological sites (e.g., settlements, farms, and luxury agricultural estates) were located in different geomorphological settings, including plains, plain–mountain transitional areas, intra-mountain basins, and small tributary valleys (Horejs, 2011a, 2014; Pirson, 2020, 2022). These landforms are potentially favorable for small settlements because of the proximity to fertile floodplains for agriculture and mountains for horticulture or pastoralism (Sommerer, 2008; Yang et al., 2021). Rural areas were also highly influenced by the rising demand for agricultural products during the period of transformation (Knitter, 2013; Laabs and Knitter, 2021). Hence, the investigation of rural catchments is integral to developing a complete picture of Pergamon's history on both very local and micro-regional scales.

Previous geoarchaeological studies in the micro-region have had different foci on selected archaeological sites, including the geomorphological investigation of prehistoric settlement locations in the Gümüş catchment (Knitter, 2013); the Geyikli valley (Schneider et al., 2013) and the landscape evolution around a hill-top settlement (Schneider et al., 2014); Bakırçay floodplain dynamics related to archaeological sites (Schneider et al., 2015, 2017); the ancient harbor city of Elaia, with studies of its

development and paleoenvironmental conditions (Seeliger et al., 2013, 2014, 2017, 2019; Pint et al., 2015; Shumilovskikh et al., 2016); the marine seismic investigation of the ancient harbor of Kane (Fediuk et al., 2019); and geophysical investigations on a monumental tumulus (Mecking et al., 2020).

Notwithstanding this relatively intensive research program, no study in the micro-region covers a continuously occupied settlement chamber that allows for the reconstruction of local geomorphodynamics in the *longue durée*. In addition, the micro-region shows remarkable diversities in relief, drainage network, and sediment accumulation in different landscape units (Yang et al., 2021), but not all of these landforms have been geoarchaeologically studied. The metadata analyses of ^{14}C ages from the western Pergamon micro-region suggest past geomorphodynamics are more or less associated with the general—but spatially more fragmented—settlement history of the region (Becker et al., 2020a). Hence, additional research, especially in the Yunt Dağı Mountains (the southern part of the micro-region), is required to fill this gap and develop a deeper understanding of the whole area.

Tekkedere catchment was therefore selected as our study area to understand human–environment interactions in the Pergamon micro-region. Archaeological remains suggest the lower Tekkedere valley was continuously settled since the Middle Bronze Age (since ca. 1700 BC) (Ludwig, 2020a; Michalski, 2021). Its settlement history thus covers the main phases of intensified human impacts on Mediterranean landscapes during the Late Holocene (Dusar et al., 2011).



Figure 1. Topography and previous geoarchaeological study sites of the Pergamon micro-region. The inset map indicates the location of this study in the Aegean coastal region of western Turkey. Abbreviations: T., Tepe; Yeni Y.T., Yeni Yeldeğirmen-tepe; Sultant., Sultantepe.

As the backbone of geoarchaeology, sediments and soils hold enormous amounts of information concerning landscape evolution and human usage history that can be accessed through various sediment analyses and chronological datings (Goldberg and Macphail, 2006). Different sediment archives might react separately to certain triggers on multiple temporal and spatial scales (e.g. Goldberg and Macphail, 2006; Duser et al., 2011; Nykamp et al., 2021). Among them, alluvial (and colluvial) deposits near ancient settlements in lower-order watersheds hold the benefit of a more direct interpretation of causal relationships between human disturbance and sediment accumulation (Dotterweich, 2008; Duser et al., 2011). With the availability of archaeological data, climatic and anthropogenic influences on geomorphodynamics can be more easily differentiated (Pérez-Lambán et al., 2018).

Our main objectives are (1) reconstructing the geomorphodynamics of the Tekkedere valley and its alluvial fan using sediment analyses and radiocarbon dating and (2) elucidating the potential drivers of the increasing geomorphodynamics, including the regional climate change and the local human impact (changing settlement pattern), in relation to supraregional Holocene records. The term “geomorphodynamics” used in this study refers to the surface changes of the Earth and related processes (Sauer and Ries, 2008; Becker et al., 2020a). In particular, it covers erosion and deposition in the terrestrial environments in our study.

Study area

Natural setting

Tekkedere catchment (ca. 13 km² drainage basin area) is a mountainous sub-catchment (second order) of the western lower Bakırçay River catchment (Fig. 1). The Bakırçay catchment (3382 km²) is under the territory of the Pergamon micro-region (Yang et al., 2021). It is one of the most fundamental river networks in Aegean Anatolia (Kayan, 1999; Yang et al., 2021). The modern climate is a typical Mediterranean subhumid climate that is characterized by dry and hot summers and mild and wet winters (Peel et al., 2007). The average annual precipitation was 749 mm and the temperature was 14.7°C during 1981–2010 in Bergama (the modern name of Pergamon) (Yang et al., 2021).

The Tekkedere catchment is adjacent to the major route network between the city of Pergamon and its ancient harbor of Elaia (Pirson, 2008; Ludwig, 2020b) with short travel distances (around 18 km and 7 km, respectively) (Fig. 1). Modern Tekkedere village is also close to ancient settlements of Teuthrania (Kalarga Tepe, ca. 8 km in the north) (Gehrke, 2014; Zimmermann et al., 2015; Williamson, 2016), Halisarna (Eğrigöl Tepe, ca. 9 km in the northeast) (Pirson, 2008; Zimmermann et al., 2015; Pavúk and Horejs, 2018), and the ancient polis of Atarneus (16 km in the northwest) (Pirson and Zimmermann, 2014; Zimmermann et al., 2015).

Geologically, the Pergamon micro-region is located in the western Extensional Province of Anatolia, which is regarded as one of the most rapidly extending regions on Earth (Özpolat et al., 2022). The NE-striking Miocene Zeytindağ and Örenli-Eğiller Grabens and the Plio-Pleistocene Bergama Graben formed under tectonic stress (Bozkurt, 2003; Yang et al., 2021). Subsidence of the grabens of Zeytindağ and Bergama (Bakırçay) is ongoing, at a rate lower than 1 mm/yr, which has resulted in a steadily rising local sea level during the Holocene (Seeliger et al., 2017). Part of the Zeytindağ Graben (Yılmaz et al., 2000; Fig. 1), the upper Tekkedere catchment, is characterized by

slightly rolling plains and shallow depressions (Yang et al., 2021). Within the catchment, Pleistocene tectonics formed NE-trending strike-slip faults (Yılmaz et al., 2000; Emre et al., 2011a, 2011b); more (unspecified or inferred) faults are reported with the NE or NW trend (modified after Yang et al. [2021] based on MTA [2002]; Fig. 2B). The bedrock in the catchment is composed of Miocene continental clastic rocks (ca. 61% of the catchment), Permian carbonate rocks with occasionally occurring clastic rocks (ca. 38% of the catchment), and pyroclastic rocks (ca. 1% of the catchment) (MTA, 2002; Fig. 2B). Reddish-brown and red Mediterranean soils develop on the clastic and pyroclastic rocks, whereas Rendzinas form on the carbonate rocks (Danacıoğlu and Tağıl, 2017).

Tekkedere creek encompasses several intermittent drainage systems (Fig. 2A) with a torrential flow regime that are similar to the other small rivers along the Aegean coast (Kayan and Vardar, 2007). There are two major creeks in the catchment. Creek A, the longest drainage way in the valley, flows from the intramountainous basin of the headwater area to the gorge, south of Kuyulu Kaya Tepe (summit ca. 160 m above sea level [m asl]). Creek B drains the northern part of the catchment (east of the Yıldız Tepe, summit ca. 210 m asl) and joins with creek A west of the Kuyulu Kaya Tepe. They continue westward as the Tekkedere creek. The creek is channelized on its alluvial fan and drains into the Bakırçay River just 12 km upstream of its mouth into the Aegean Sea.

The slopes of the lower valley (including the valley of creek B) are asymmetrical (Ludwig, 2019; Fig. 2C). The northern slopes are steeply inclined (16–37°, mean = 20°), whereas the southern slopes are gentler (10–30°, mean = 15°). Strong denudation and soil erosion are the prevailing geomorphological processes on the southern slopes, partly confined by agricultural terraces grown with olives (Becker et al., 2020b; Fig. 2A and C). Where soils are fully eroded, scattered bare rocks crop out, mainly on the southern slopes (Ludwig, 2019; Fig. 2A). The Kuyulu Kaya Tepe has large areas of outcropping bedrock with scree covering its southern footslopes.

Locally, the tributaries of Tekkedere creek are incised for more than 1 m into the valley infills (Fig. 2C). The valley bottom widens in its lower course where the modern Tekkedere village is built on its right riverbank (Fig. 2A). The Tekkedere alluvial fan forms at the opening area from the valley to the Bakırçay floodplain, covers an area of ca. 2 km² (length: ca. 2 km; width: ca. 1.4 km), and is the largest alluvial fan in the foreland of the western Yunt Dağı Mountains. The altitude difference from the fan's apex to its toe amounts to 18 m, which is calculated based on TanDEM-X data (Wessel et al., 2018). At present, the toe of the fan is located only ca. 500 m east of the current Bakırçay River channel (Fig. 2A).

While arable lands with vegetable and grain cropping dominate the land use in the headwater area of Tekkedere valley, coniferous forests, transitional woodland–shrubland covers, and olive groves on agricultural terraces characterize the vegetation cover on the slopes of the middle valley (Supplementary Fig. 1 based on Corine Land Cover data [Cole et al., 2018] and field observations). In the lower part, pine forests cover the northern slopes (Yıldız Tepe), whereas olives are mainly cultivated on the southern slopes and the valley bottom. Olive cultivation characterizes the upper part of the Tekkedere alluvial fan. Downslope, at the fan's apex, at the middle and distal fan, cotton and vegetable cropping predominates, and fig and citrus fruit trees occur sporadically.

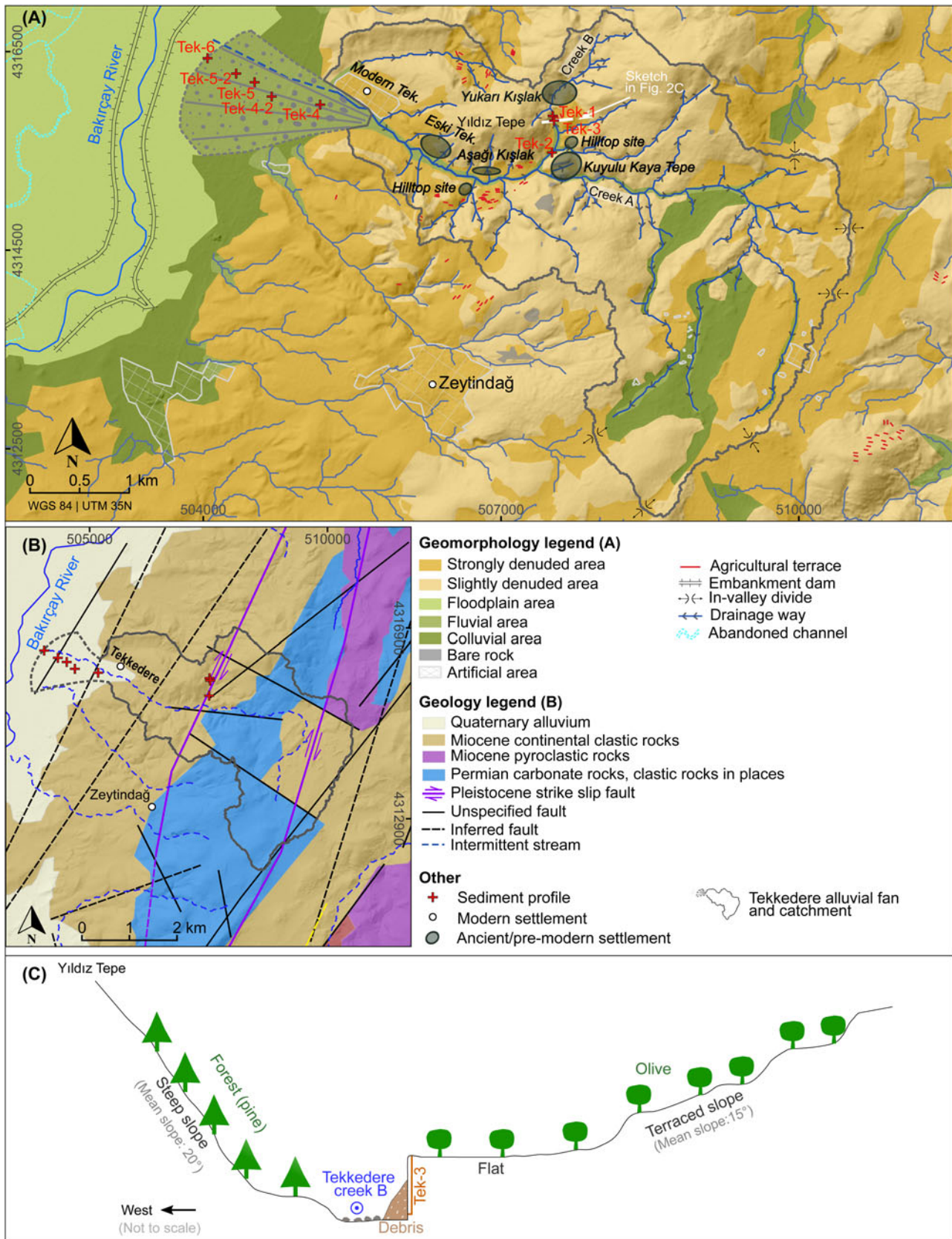


Figure 2. Overview of the Tekkedere area. (A) Geomorphological map of the Tekkedere area with locations of the sediment profiles and settlements (Ludwig, 2019, 2020a; Michalski, 2021). (B) Geological map of the Tekkedere area (modified after Yang et al. [2021] based on MTA [2002] and Emre et al. [2011a, 2011b]). (C) Schematic cross-section through the Tekkedere creek B (located at the sediment profile Tek-3).

A palynological study around Elaia indicates the vicinity of Tekkedere was dominated by natural deciduous oak forests between 7.6 and 3 ka BP (Shumilovskikh et al., 2016). Deforestation occurred as a consequence of the increased layout of olive groves and the development of macchia shrublands under rising grazing pressure since the Hellenistic Period, reaching a maximum during 2.1–1.8 ka BP. Alongside the hillslopes, semi-natural forests (mainly pines) developed during the past millennium (Shumilovskikh et al., 2016). The abundance of grains and the fertility of the area were described by ancient geographers and historians (Sommerer, 2008; Pirson and Zimmermann, 2014). Recent studies, however, suggest that Pergamon's demand for grain, at least in the Roman Imperial Period, could not be covered without imports or environmental modifications (e.g., agricultural terracing) (Kobes, 1999; Günther et al., 2021; Laabs and Knitter, 2021).

Settlement history

Since 2018, archaeological surveys have been conducted in the Tekkedere catchment by the German Archaeological Institute (Deutsches Archäologisches Institut [DAI]) (Ludwig, 2019, 2020a). Their findings provide evidence of at least six archaeological sites in the catchment (Fig. 2A), indicating almost uninterrupted settlement continuity and changing settlement patterns since the late Middle Bronze Age (ca. 1700 BC) (Ludwig, 2019, 2020a; Michalski, 2021).

Ceramic remains on and around the hill site of Kuyulu Kaya Tepe (Um19 Fst 02) (Fig. 2A) indicate settlement activities continued from the late Middle Bronze Age to the end of the Early Byzantine Period (ca. 3.7–1.2 ka BP) (Ludwig, 2019; Michalski, 2021). Building remains, including several cisterns, have been found on the rock plateau (Ludwig, 2019). A small rural settlement that probably reached its peak during Classical antiquity was situated at the footslopes of Kuyulu Kaya Tepe. Considering that the Kuyulu Kaya Tepe surmounts the surroundings by ca. 40 m and is characterized by steep slopes with outcropping bedrock toward creek A, the site, especially the hill site on the rock plateau, might have been used as a fortress to overlook or control the entire Tekkedere valley and large parts of the western lower Bakırçay plain (Ludwig, 2020a; Fig. 2A).

Two small hilltop sites (UM19 Fst 04 and 13), a few hundred meters to the north and west of the Kuyulu Kaya Tepe along creek B (Fig. 2A) with a high concentration of ceramics and bricks, suggest human activities took place during Classical antiquity (Ludwig, 2020a).

The predecessor settlement of the modern Tekkedere village was likely first established as the upper settlement (Yukarı Kışlak; UM18 Fst 01 or UM19 Fst 09), ca. 1 km north of the Kuyulu Kaya Tepe along creek B (Ludwig, 2019; Fig. 2A). Based on the archaeological results, the upper settlement duration is assumed to have been from late antiquity to the Byzantine Period (Ludwig, 2020a). The settlement was replaced by the smaller lower settlement (Aşağı Kışlak; UM19 Fst 14) which was situated in the middle of the lower valley (Ludwig, 2020a; Tozan, 2022; Fig. 2A). When the lower settlement was abandoned, the old Tekkedere settlement (Eski Tekkedere) was built farther downstream (Tozan, 2022). The old Tekkedere settlement was given up mostly due to an earthquake-triggered landslide, which was previously assumed to occur in the middle of the nineteenth century (Ludwig, 2020a). Based on the information provided by the locals, it was the earthquake that took place around Dikili, Zeytindağ, and Bergama in 1939 (Paradisopolou et al., 2010; Çelik et al., 2019). Residents left and developed the

modern Tekkedere village, which is built directly to the west of the old Tekkedere settlement (Ludwig, 2020a).

METHODS

Fieldwork

Three sediment outcrops along the banks of creek B were described and sampled in September 2019 (Becker et al., 2020b), and five sediment cores were extracted and brought to the surface along a transect from the apex to the toe of the alluvial fan by vibracoring (Wacker BHF 30 S, with 5-cm-diameter open cores) in October 2020 (Becker et al., 2022; Fig. 2A, Table 1). None of the profiles reached the underlying bedrock.

Lithostratigraphy was documented as comprising sediment color (Munsell soil color), unit thickness, sediment depositional structure (Stow, 2005), sediment texture and fabric (Blair and McPherson, 1999), hydromorphic feature, biological modification, and occurrence of artifacts (Jahn et al., 2006). The degree of reaction to 9.9% HCl was applied as an indicator for the amount of calcium carbonate (CaCO₃) (Jahn et al., 2006). A summary classification of the sediment description can be found in Yang et al. (2022). Sediment samples (3- to 5-cm-thick pieces, n = 191) for geochemical analyses were collected according to the unit thickness and their position to unit. Sediment profiles were carefully checked for charcoal pieces and bulk samples containing organic matter for radiocarbon dating.

Laboratory work

Sediment analyses

Geochemical analyses of sediments can effectively assist in distinguishing the occurrence of past soil formation and the difference in natural and cultural processes (Terry, 2017). Sediment samples were analyzed in the laboratory of the Bergama archaeological excavation house. Before the measurement, samples were air-dried for more than 48 h, and the aggregates were crushed in a porcelain mortar. For subsequent analyses, the fine fraction ($\varnothing < 2$ mm) was separated from the coarse component by dry sieving.

The pH and electrical conductivity (EC) values were obtained in the water-saturated sediments (1:2.5 solutions of 5 g of sediment and 12.5 mL of distilled water) with a TDS/EC/pH/TEMP meter (EZ9908; resolution: 0.01 pH, 1 μ S/cm EC). Reaction class terms and the pH range are based on the soil survey manual (Soil Science Division Staff, 2017; Table 2). The pH value in sediment solutions is highly related to the buffering process of organic acids and is indicative of paleosol occurrence (Nykamp et al., 2020) and human activity (Terry, 2017). The EC value provides a hint of readily soluble salts that crystallize from chemical weathering or soil water evaporites (Nykamp et al., 2020).

Approximately 10 g of oven-dried (105°C) sediments were measured using loss on ignition at 550°C (LOI₅₅₀) (Dean, 1974; Heiri et al., 2001). LOI₅₅₀ was calculated as the weight difference of a sample treated at both temperatures and is used for the estimation of organic matter content (Heiri et al., 2001; Santisteban et al., 2004). The in-lab reference material was measured after every 20 sample batch to control variability, which is reproducible with a median LOI₅₅₀ value of 5.6 mass% (median absolute deviation [MAD]: 0.2 mass%). Often, a higher LOI₅₅₀ value is associated with oxidation accumulation, pointing to soil horizons, the stability of land surface, and the intensity of human activity (Goldberg and Macphail, 2006; Panin et al., 2021).

Table 1. Metadata of sediment outcrops in the valley (n = 3) and drilling cores on the alluvial fan (n = 5) of the Tekkedere catchment (WGS 84).

Sediment sequence	Latitude (°N)	Longitude (°E)	Elevation (m asl)	Depth (cm)	Samples (n)	Geomorphological position	Land use
Tek-1	38.99164	27.08685	88.7	176	14	Valley (channel bank)	Olive grove
Tek-2	38.98832	27.08677	70.8	158	11	Valley (channel bank)	Olive grove
Tek-3	38.99120	27.08701	84.0	220	19	Valley (channel bank)	Olive grove
Tek-4	38.99268	27.05971	16.6	200	0	Alluvial fan (apex)	Olive grove
Tek-4-2	38.99341	27.05418	11.5	700	32	Alluvial fan (middle)	Arable land
Tek-5	38.99472	27.05216	9.1	786	48	Alluvial fan (middle)	Arable land
Tek-5-2	38.99554	27.04988	7.4	400	17	Alluvial fan (middle)	Arable land
Tek-6	38.99688	27.04662	6.3	800	50	Alluvial fan (toe)	Arable land

Table 2. The equal interval classification of the sediment proxies (except pH; Soil Science Division Staff, 2017).^a

Class	pH	EC (µS/cm)	X _{LF} (10 ⁻⁸ m ³ /kg)	LOI ₅₅₀ (mass%)
Class 1 (very low)	6.5–7.3	Neutral	84–227	4–32
Class 2 (low)	7.3–7.8	Slightly alkaline	227–371	32–60
Class 3 (medium)	7.8–8.4	Moderately alkaline	371–515	60–87
Class 4 (high)	8.4–9	Strongly alkaline	515–659	87–115
Class 5 (very high)	≥ 9	Very strongly alkaline	659–803	115–143

^aEC, electrical conductivity; LOI₅₅₀, loss on ignition at 550°C; X_{LF}, mass-specific susceptibility at the low frequency.

The magnetic susceptibility of sediments was measured with a Bartington magnetic susceptibility system (MS3 meter and MS2B dual-frequency sensor; measuring resolution: 2×10^{-6} SI; range: 26 SI) using the Bartsoft software. The volume-specific magnetic susceptibility (κ) at low frequency (LF, 0.46 kHz) of samples weighed using 12 cm³ plastic pots was determined with triple repetition. The mass-specific susceptibility at the low frequency (X_{LF}, 10⁻⁸ m³/kg) was calculated according to Dearing (Dearing, 1994; Dearing et al., 1996). The confidence intervals of sample median X_{LF} values were estimated by simple quantile bootstrapping (B = 1000) in R v. 3.6 (R Core Team, 2021). In addition, we used the MS2B meter to measure the Tek-5 samples (n = 48) five times. The results are highly comparable to 88% of samples used via the MS3 meter (correlation of the sediment measured in both meters: median = 0.97). The median of the volume-specific susceptibility of the 10 mL calibration sample is 2620×10^{-5} SI (MAD: 0.25×10^{-5} SI; accuracy: 1%). Higher X_{LF} values are generally related to the formation of clay minerals under a higher weathering process (Maher and Thompson, 1991; Blundell et al., 2009; Sherriff, 2014).

The elemental composition of sediment samples from the profiles of Tek-5, Tek-5-2, and Tek-6 was analyzed using a portable energy-dispersive X-ray fluorescence spectrometer (p-ED-XRF; Thermo Fisher Scientific NITON XL3t) measuring each sample for 120 s in the manufacturer's Mining Cu/Zn mode with main, high, low, and light filters (50, 50, 15/20, and 8 kV, respectively). The certified reference material (LKSD-4) (Lynch, 1990) and the acid-purified silica sand were taken as standards to ensure measurement quality. The reproducibility of selected elements (Zr, Rb, Ti, and Ca) for LKSD-4 and silica sand are in ranges of 22–34% and 6–11%, respectively. Two element ratios were calculated for sediment characterization. The Zr/Rb ratio is

used as a proxy for grain-size variability (Dinelli et al., 2007) and the Ca/Ti ratio as an indicator for syndimentary weathering as well for the precipitation of secondary carbonates (Ülgen et al., 2012).

The sediment proxies in this study are reported in median and MAD (in parentheses) values and are grouped using an equal interval classification of the data (Table 2). Raw/processed data and R code (R Core Team, 2021) can be found in the data set in Pangaea (Yang et al., 2022).

Radiocarbon dating

In our study, radiocarbon dating would be the optimum solution for the development of a chronological framework due to the scarcity of available materials for alternative methods. Accelerator mass spectrometry (AMS) radiocarbon dating (¹⁴C) of samples was conducted at the TÜBİTAK National 1 MV AMS Laboratory (Doğan et al., 2021). Dated materials (n = 20) include charcoals, the mixture of mainly charcoal with adjacent sediments (if %C of the macroscopically separable charcoal is <1–2 mg), organic-rich bulk samples, and one terrestrial snail shell (Table 3).

Macroscopic plants and rootlets were removed from the samples before the standard pretreatment procedure (acid-base-acid [ABA] protocol) was applied (Fowler et al., 1986; Bronk Ramsey, 2008; Brock et al., 2010). Fragile charcoal remnants with an amount of charcoal below ca. 10 mg were only treated with an acid wash (Fowler et al., 1986; Brock et al., 2010). The radiocarbon ages were calibrated via the IntCal20 calibration curve (Reimer et al., 2020) and the rcarbon package (Crema and Bevan, 2021) in R v. 3.6 (R Core Team, 2021). We report a 95% probability range for the calibrated ages.

Table 3. The AMS-¹⁴C dating samples from the Tekkedere valley (n = 6) and Tekkedere alluvial fan (n = 14), pretreatment procedure, sediment facies of the sample location and their dating results and calibration (calibration curve: IntCal20; Reimer et al., 2020).

Sediment profile	Depth/cm bs (unit ID) ^a	Lab. ID (TÜBİTAK*)	Dated material ^b	Pretreatment procedure ^c	Sediment facies ^d	Radiocarbon age ¹⁴ C yr BP ± σ	cal yr BP		BC/AD (95%)
							Median	95% probability	
Tek-1	40 (㉔)	1143	Charcoal	ABA	Ab	318 ± 23	388	456–308	AD 1494–1642
	144 (㉔)	1145	Shell	Acid splash	Aa	663 ± 24	628	668–560	AD 1282–1390
	172 (㉔)	1142	Charcoal	ABA	Ab	627 ± 24	599	653–554	AD 1297–1396
Tek-2	65 (㉔)	1144	Charcoal	ABA	sAa	899 ± 23	791	904–732	AD 1046–1218
	75–80 (㉔)	1141	Charcoal	ABA	sAa	910 ± 24	827	908–737	AD 1042–1213
Tek-3	125 (㉔)	1140	Charcoal	ABA	Ab	1243 ± 26	1183	1271–1072	AD 679–878
Tek-4-2	161 (㉔)	1646	C/S	ABA	Bb	4164 ± 28	4708	4829–4581	2880–2632 BC
	469 (㉔)	1647	C/S	Acid wash	sBa	4283 ± 45	4852	4971–4653	3022–2704 BC
	221 (㉔)	1648	C/S	Acid wash	Ba	5680 ± 31	6457	6556–6396	4607–4447 BC
Tek-5	260–265 (㉔)	1649	C/S	Acid wash	Ba	4719 ± 29	5447	5575–5325	3626–3376 BC
	363 (㉔)	1650	C/S	Acid wash	Bb	3399 ± 27	3634	3812–3566	1863–1617 BC
	427 (㉔)	1651	Bulk soil	Acid wash	sCf	4330 ± 30	4892	4968–4841	3019–2892 BC
	435 (㉔)	1652	C/S	Acid wash	sCf	4635 ± 27	5412	5462–5309	3513–3360 BC
	478 (㉔)	1653	Bulk soil	Acid wash	sCf	5347 ± 30	6128	6270–6002	4321–4053 BC
	781 (㉔)	1654	Charcoal	ABA	Cf	4502 ± 31	5162	5301–5045	3352–3096 BC
	273 (㉔)	1655	Charcoal	Acid wash	Ba	2542 ± 26	2627	2743–2499	794–550 BC
Tek-5-2	285–286 (㉔)	1656	Bulk soil	Acid wash	sCf	3734 ± 31	4086	4224–3982	2275–2033 BC
	354 (㉔)	1657	C/S	ABA	Cf	5046 ± 28	5823	5901–5718	3952–3769 BC
Tek-6	459–460 (㉔)	1658	Bulk soil	Acid wash	Cs	4308 ± 29	4861	4959–4833	3010–2884 BC
	665–666 (㉔)	1659	Bulk soil	Acid wash	Cs	5294 ± 29	6082	6187–5947	4238–3998 BC

^acm bs, cm below surface. Numbers in circles correspond to unit numbers in Figs. 3–5.^bC/S refers to mixed materials (charcoal and accompanying sediments).^cABA refers to standard acid-base-acid protocol.^dSee Table 4 for descriptions.

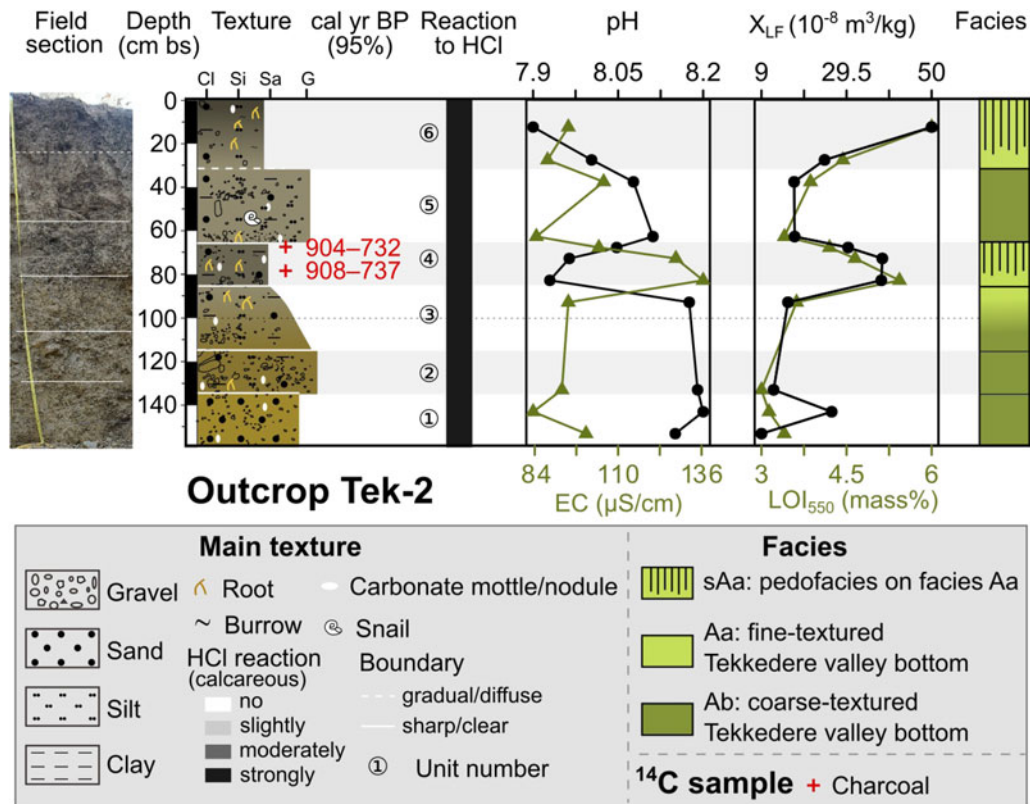


Figure 3. The lithostratigraphy, radiocarbon dates, and sedimentological analyses of sediment outcrop Tek-2. The color of the sediment texture column represents the color observed in the field; the shaded band represents the different units and the dashed line refers to the depth in every meter. cm bs, cm below surface; EC, electrical conductivity; LOI_{550} , loss on ignition at 550°C; X_{LF} , mass-specific susceptibility at the low frequency.

SEDIMENT CHARACTERISTICS

The analyzed sediment profiles are located in two different landforms: the valley infill of the tributary creek B and the Tekkedere alluvial fan (Table 1). Profile Tek-2 from the valley infill and profiles Tek-5 and Tek-6 from the fan are taken as key profiles and are presented in detail. Additional profiles provided in the Supplementary Material show comparable sediment characteristics. The calculation of the median value of sediment proxies from different profiles' sedimentary units is provided in the data set (Yang et al., 2022). Taken together, the samples' ages range between ca. 6.6 and 0.3 cal ka BP (Table 3).

Tekkedere valley infill: key profile Tek-2

Profile Tek-2 has a total thickness of 158 cm, and its six lithostratigraphic units are dominated by alternating units of silts/sands and pebbles (Fig. 3). Except for the upper two units (units 5 and 6), lithostratigraphic units 1–4 show sharp contacts. Roots occur commonly above 100 cm below surface (cm bs). The sediment matrix is strongly calcareous and moderately alkaline (pH: 8.1 (0.1)). EC values (EC: 95 (10) $\mu\text{S}/\text{cm}$) are very low (class 1; Table 2) and only slightly increased in unit 4. X_{LF} (24 (9) $\times 10^{-8} \text{ m}^3/\text{kg}$, class 1) and LOI_{550} (4.1 (0.6) mass%, class 3) peak in the same unit.

Basal unit 1 (158–135 cm bs) is characterized by yellowish-brown, highly compacted silty sand with few embedded medium pebbles ($\varnothing < 2$ cm). Some pebbles show a grayish weathering rind.

Unit 2 (135–116 cm bs) shows clast-supported fabric. The clasts consist of yellowish-brown, disorganized pebbles with few fine cobbles ($\varnothing < 11$ cm). The matrix is sandy silt with adhesions of secondary precipitated carbonates and very few fine roots.

Unit 3 (116–84 cm bs) is characterized by normally graded fabric. The sediment texture changes from strong yellowish silty sand with few angular, disorganized fine to coarse pebbles ($\varnothing < 3$ cm) at the base of the unit, to light gray silty sand at the top. Clasts are partly carbonated and slightly weathered. Very few fine to coarse roots occur throughout the unit. The analytical values of sediment samples ($n = 4$) from units 1–3 remain roughly constant. Sediments are moderately alkaline (pH: 8.2 (0)). EC (94 (4) $\mu\text{S}/\text{cm}$, class 1) and X_{LF} (14 (3) $\times 10^{-8} \text{ m}^3/\text{kg}$, class 1) are very low. LOI_{550} (3.4 (0.2) mass%, class 2) is low.

Unit 4 (84–65 cm bs) is composed of light grayish, slightly sandy silt with few fine pebbles. Fine roots and burrows are abundant. Sediments are moderately alkaline and enhanced in solutes (EC: 128 (9) $\mu\text{S}/\text{cm}$, class 1, $n = 3$). X_{LF} amounts to 38 (0) $\times 10^{-8} \text{ m}^3/\text{kg}$ (class 2, $n = 3$), and LOI_{550} totals to 4.9 (0.5) mass% (class 4, $n = 3$). Two charcoal pieces (at 65 cm bs and 75–80 cm bs) date unit 4 to around 908–732 cal yr BP (Fig. 3, Table 3).

Unit 5 (65–32 cm bs) is characterized by light grayish, silty sand with embedded pebbles to fine cobbles ($\varnothing < 7$ cm). A thin rooted clast-supported layer of fine pebbles is interbedded at 65–60 cm bs. A shell of a land snail occurs at 55 cm bs EC, X_{LF} , and LOI_{550} values ($n = 2$) widely correspond to the values of units 1–3.

Unit 6 (32–0 cm bs) corresponds to the modern plow horizon. It consists of dark to light brown sandy silt with very few fine to coarse pebbles ($\varnothing < 3$ cm). The unit has abundant roots and common burrows. The samples ($n = 2$) show slightly decreased pH values (7.9 (0.1)) and increased X_{LF} (37 (13) $\times 10^{-8} \text{ m}^3/\text{kg}$, class 2) and LOI_{550} (5.5 (0.8) mass%, class 4) values.

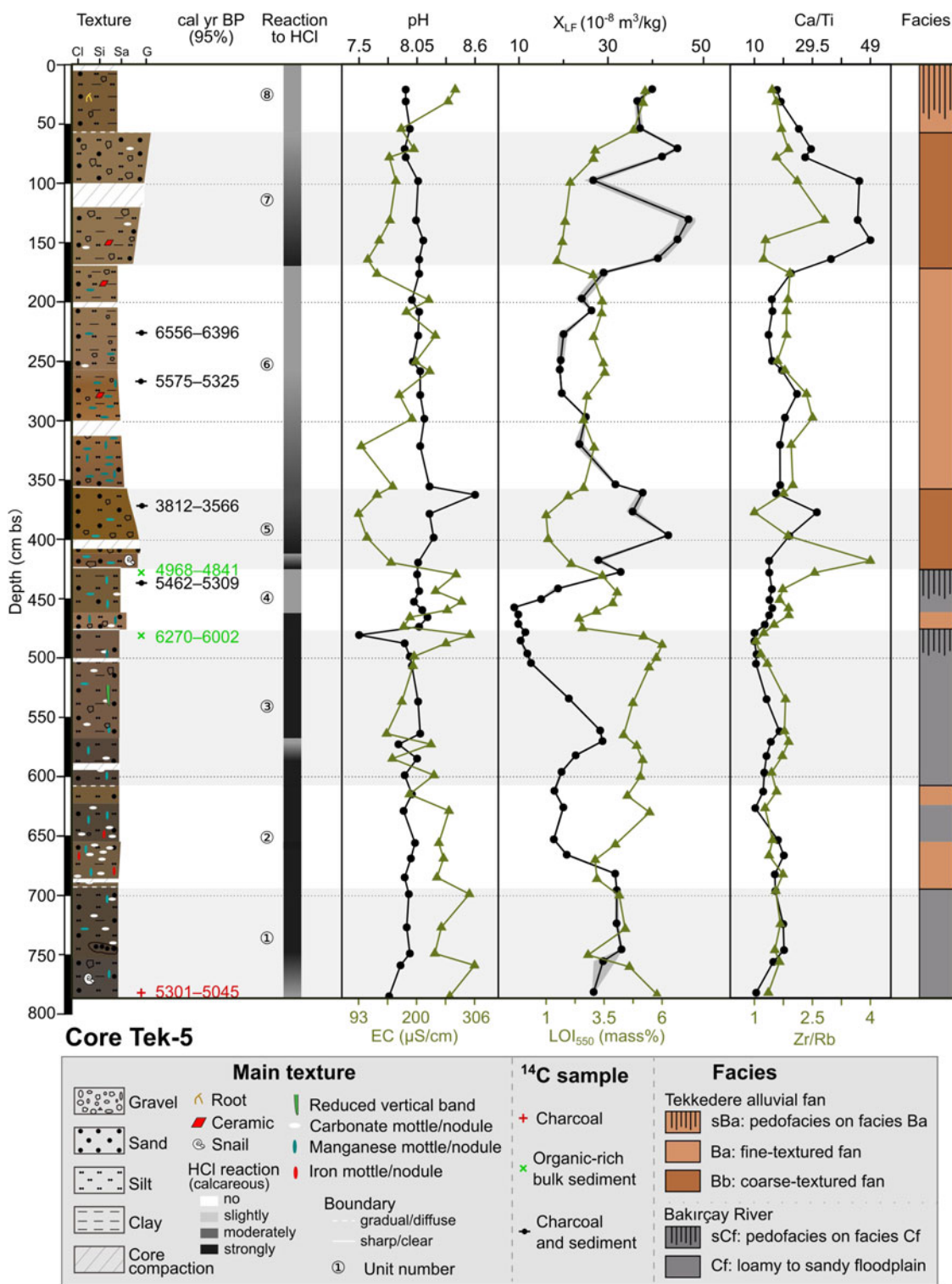


Figure 4. The lithostratigraphy, radiocarbon dates, and sediment analyses of sediment core Tek-5. The confidence intervals of the sample median mass-specific susceptibility at the low frequency (X_{LF}) values are estimated by simple quantile bootstrapping ($B=1,000$). cm bs, cm below surface; EC, electrical conductivity; LOI_{550} , loss on ignition at 550°C.

Tekkedere mid-fan: key profile Tek-5

Profile Tek-5 was obtained from the middle position of the Tekkedere alluvial fan (Fig. 2A). The extracted 786-cm-thick sediment sequence is divided into eight units (Fig. 4). The lower part of the profile (below 426 cm bs, units 1–4) is mainly characterized

by layers of dark grayish or brownish silts with very few embedded fine pebbles, whereas units of brownish silts and sands with variable contents of pebbles prevail in the upper half of the profile (units 5–8). Concentrations of secondary precipitated carbonates and manganese mottles or small nodules occur almost throughout the whole profile.

Sediment samples ($n = 48$) in the profile Tek-5 are slightly to strongly alkaline (pH: 8.0 (0.1)). EC indicates an overall very low amount of solutes (195 (43) $\mu\text{S}/\text{cm}$, class 1, $n = 48$) with slightly increased values in units 1–4 (237 (35) $\mu\text{S}/\text{cm}$, class 2, $n = 25$). X_{LF} shows a median value of $27 (7) \times 10^{-8} \text{ m}^3/\text{kg}$ (class 1, $n = 48$) with relatively low results in units 1–4 ($20 (8) \times 10^{-8} \text{ m}^3/\text{kg}$, class 1, $n = 25$) and relatively high results in units 5–8 ($32 (7) \times 10^{-8} \text{ m}^3/\text{kg}$, class 2, $n = 23$). LOI_{550} has a median value of 3.5 (0.9) mass% (class 3, $n = 48$) in the profile, with slightly higher values in units 1–4 (4.4 (0.7) mass%, class 3, $n = 25$) than in units 5–8 (3.2 (0.4) mass%, class 2, $n = 23$). Ca/Ti and Zr/Rb ratios also display marked differences between the upper and lower halves of the profile. Variabilities of both Ca/Ti (14.70 (2.1), $n = 25$) and Zr/Rb (1.50 (0.2), $n = 25$) in units 1–4 are slightly smaller than in units 5–8, where Ca/Ti has a median value of 19.99 (4.4, $n = 23$) and Zr/Rb has a median value of 1.71 (0.2, $n = 23$) (Fig. 4). In addition to sedimentological differences between the two parts of the profile, differences are also identified among the units. Dating results in Tek-5 ($n = 7$, from ca. 6.6 cal ka BP at 221 cm bs to 3.6 cal ka BP at 363 cm bs) show markedly repeated age inversions (Fig. 4, Table 3).

Unit 1 (786–693 cm bs) consists of very dark gray (10YR 3/1), moderately to strongly calcareous sandy silt. An intermediate sandy layer occurs at 751–740 cm bs. Common carbonate nodules and few manganese mottles exist. Fine pieces of snail shells were found around 765 cm bs. The charcoal sample from the bottom of the profile (781 cm bs) dates to 5301–5045 cal yr BP (Table 3). The transition from unit 1 to 2 takes place gradually.

Unit 2 (693–607 cm bs) contains two layers of dark yellowish-brown (10YR 4/3) sandy silt with an intercalated layer of very dark grayish-brown (10YR 3/2) sandy silt at 658–662 cm bs. Sediments are strongly calcareous. Few blackish manganese and reddish iron nodules ($\varnothing < 1 \text{ cm}$) and common carbonate nodules occur in the lower third of the unit. The sediment boundary between units 2 and 3 is gradual.

Unit 3 (607–477 cm bs) consists of strongly calcareous sandy silt with very few fine pebbles. The color changes from dark brown (7.5 YR 3/2) at the bottom to brown (7.5 YR 4/3) at the top. Few fine carbonate nodules and manganese mottles are incorporated. One vertical greenish mottled structure occurs at 530–520 cm bs.

Bulk parameters of LOI_{550} and X_{LF} display strong oscillations in median values for the three units (Fig. 4). In unit 1, X_{LF} has a median value of $32 (2) \times 10^{-8} \text{ m}^3/\text{kg}$ (class 2, $n = 5$), and the median value of LOI_{550} ranges into class 3 (4.4 (0.2) mass%). With decreasing depth in unit 2, LOI_{550} values slightly increase, while values for X_{LF} slightly decrease (Fig. 4). Small peaks in X_{LF} and LOI_{550} occur at the intermediate layer of unit 2. In unit 3, X_{LF} values ($n = 9$) peak at 570 cm bs ($29 \times 10^{-8} \text{ m}^3/\text{kg}$, class 1) and gradually decrease toward the top, reaching a minimum value ($10 \times 10^{-8} \text{ m}^3/\text{kg}$, class 1) at 480 cm bs. LOI_{550} values gradually increase from 5 to 5.8 mass% (class 4) with decreasing depth. At the top of unit 3 (478 cm bs), the organic-rich bulk sample dates to 6270–6002 cal yr BP. The boundary between unit 3 and overlying unit 4 is sharp.

Unit 4 (477–426 cm bs) is composed of brown (7.5 YR 5/4), poorly compacted and strongly calcareous, slightly fine pebbly, silty sand in the lower part (477–463 cm bs) and dark yellowish-brown (10YR 4/4), heavily compacted, moderately calcareous sandy silt in the upper part (463–426 cm bs). Some pebbles are carbonated. Few fine manganese nodules and very few fine carbonate concretions were found.

The median pH value of water-saturated sediments in unit 4 is around 8.1 ($n = 6$) and is in the same range as the underlying units (moderately alkaline). Also, EC values are comparable to those in the underlying sediments but exhibit remarkable oscillations (245 (32) $\mu\text{S}/\text{cm}$, class 2, $n = 6$). LOI_{550} is low in the lower layer of unit 4 (2.7 mass%, class 2, at 477–463 cm bs), and it increases toward the unit top, peaking at 444 cm bs (4.1 mass%, class 3). X_{LF} has a median value of around $13 (3) \times 10^{-8} \text{ m}^3/\text{kg}$ (class 1, $n = 6$) and constantly increases from $10 \times 10^{-8} \text{ m}^3/\text{kg}$ (class 1) at the bottom to $33 \times 10^{-8} \text{ m}^3/\text{kg}$ (class 2) at the top. Graphs of element ratios (Ca/Ti and Zr/Rb) widely run in parallel, both showing low values in the lower strata (units 1–4; Fig. 4). At the top of unit 4, a bulk sample from 427 cm bs dates to 4958–4841 cal yr BP, and a mixed charcoal/sediment sample from 435 cm bs dates to 5462–5309 cal yr BP. The boundary with overlying unit 5 is sharp.

Unit 5 (426–358 cm bs) consists of dark yellowish-brown (10YR 4/6), normally graded sediments. Sediment texture changes from very soft, subangular to subrounded medium pebbly ($\varnothing < 2 \text{ cm}$) sand at the base to silty sand at the top. A snail fragment occurs at 420 cm bs. The sediments are moderately to strongly calcareous and contain very few blackish manganese mottles. The pH peaks at the top of unit 5 (pH: 8.6, strongly alkaline, at 363 cm bs). Within unit 5 ($n = 4$), EC (118 (17) $\mu\text{S}/\text{cm}$, class 1) and LOI_{550} (1.9 (0.4) mass%, class 1) drop to their lowest values, whereas X_{LF} ($37 (4) \times 10^{-8} \text{ m}^3/\text{kg}$, class 2) shows high values in comparison with the underlying and overlying units. Element ratios of Ca/Ti (19.2 (3.4)) and Zr/Rb (1.7 (0.4)) also slightly increase compared with the lower units. The mixed charcoal/sediment sample at 363 cm bs dates to 3812–3566 cal yr BP. The boundary with overlying unit 6 is sharp.

Unit 6 (358–169 cm bs) consists of soft, moderately calcareous, and normally graded sediments. The texture changes from strongly brown (7.5 YR 4/4) sandy silt at the bottom to brown (7.5 YR 5/6) slightly sandy silt at the top. Few fine pebbles ($\varnothing < 1 \text{ cm}$) occur and very few of them are carbonated. Grayish to blackish manganese mottles commonly exist throughout the unit, particularly at 358–313 cm bs. Fine brick/ceramic fragments were found at 180 and 273 cm bs.

The measured bulk parameters ($n = 10$) remain constant in this unit and show clear differences with the underlying unit 5 and the overlying unit 7. Sediments are moderately alkaline (pH: 8.1 (0.1)). EC shows alternating, but overall increased values (186 (33) $\mu\text{S}/\text{cm}$, class 1). X_{LF} values display a distinct trough ($24 (4) \times 10^{-8} \text{ m}^3/\text{kg}$, class 2) compared with the underlying unit 5 ($37 (4) \times 10^{-8} \text{ m}^3/\text{kg}$, class 2, $n = 4$) and overlying unit 7 ($44 (2) \times 10^{-8} \text{ m}^3/\text{kg}$, class 2, $n = 6$). LOI_{550} (3.2 (0.3) mass%, class 2) remains relatively stable and is higher than in the underlying (1.9 (0.4) mass%, class 1, $n = 4$) and overlying unit (2.2 (0.3) mass%, class 2, $n = 6$). Element ratios (Ca/Ti and Zr/Rb) remain roughly the same and show relatively lower values compared with the underlying and overlying units. The two datings of mixed charcoal/sediment samples show distinct age inversions. The sample from 260–265 cm bs dates to 5575–5325 cal yr BP. The sample from 221 cm bs dates to 6556–6396 cal yr BP and, thus, is older than the underlying age samples. The transition between units 6 and 7 is sharp.

Unit 7 (169–58 cm bs) is characterized by yellowish-brown (10YR 5/4), slightly compacted, and inversely graded sediments. Sediment texture changes from fine pebbly silty sand at the bottom to sandy, subangular subrounded medium pebbles at the top. The pebbly sediments at the top are matrix-supported and

poorly sorted. Sediments in this unit are strongly calcareous and contain very few carbonate nodules. A ceramic piece occurs at 149–140 cm bs and a small brick fragment at 150–147 cm bs. Geochemical samples ($n=6$) indicate relatively low EC (150 (15) $\mu\text{S}/\text{cm}$, class 1) and LOI_{550} values (2.2 (0.3) mass%, class 2) compared with those in the overlying and underlying units. Overall, LOI_{550} values gradually increase from the bottom (1.8 mass%, class 1) to the top (3.3 mass%, class 2). Along with the whole extracted profile, values of X_{LF} ($44 (2) \times 10^{-8} \text{ m}^3/\text{kg}$, class 2) and the Ca/Ti ratio (40.05 (6.9)) reach their maximum in unit 7. Also, the Zr/Rb has a peak of 2.55 at 130 cm bs. The boundary with overlying unit 8 is gradual.

Unit 8 (58–0 cm bs) corresponds to the present-day plow horizon and contains dark yellowish-brown (10YR 4/4), moderately calcareous, slightly sandy silt with very few embedded fine pebbles and roots. The pH values remain stable all over units 6–8 (moderately alkaline). EC values steadily increase from the bottom to the top of unit 8, reaching 271 $\mu\text{S}/\text{cm}$ (class 2) at the surface. LOI_{550} contents have a median value of 5.1 (0.1) mass% (class 4, $n=3$). X_{LF} values ($37 (0) \times 10^{-8} \text{ m}^3/\text{kg}$, class 2, $n=3$) are slightly lower than in the underlying unit 7. Element ratios ($n=3$) of Ca/Ti (18.57 (1.3)) and Zr/Rb (1.50 (0.1)) are in the same range as unit 6 and are distinctly lower than unit 7.

Tekkedere fan toe: key profile Tek-6

Profile Tek-6 was extracted from the toe of the Tekkedere alluvial fan. It has a total thickness of 800 cm and includes seven units (Fig. 5). This profile is characterized by a thick (2.5 m) unit of blackish-grayish clayey silt (unit 2) in its lower part, overlain by normally graded sediments (units 3 and 4) in the middle part and brownish fine-textured sediments (units 5–7) in the upper 2 m. Sediments of Tek-6 are moderately to strongly calcareous.

The pH values in the lower half of the profile (below 427 cm bs, units 1 and 2) are constant at 8.4 (0.1, $n=30$), corresponding to a moderately alkaline environment. Sediments from 400 cm bs to the profile surface gradually change to slightly alkaline (pH is 7.9 at 33 cm bs). The graphs of EC (343 (108) $\mu\text{S}/\text{cm}$, class 2, $n=50$) and LOI_{550} values (3.9 (2.1) mass%, class 3, $n=50$) run inversely to the graph of pH values. The lowest EC and LOI_{550} values are observed at the middle profile (427–224 cm bs). The graph of X_{LF} values ($56 (29) \times 10^{-8} \text{ m}^3/\text{kg}$, class 2, $n=50$) roughly shows the same trend as pH and peaks at $109 (10) \times 10^{-8} \text{ m}^3/\text{kg}$ (class 4) in the middle part of the profile (427–224 cm bs, $n=11$). The element ratio of Ca/Ti has a median value of 12.94 (3.9) and Zr/Rb has a median value of 1.20 (0.2), with a distinct Ca/Ti peak at 677 cm bs and a distinct Zr/Rb peak at 400 cm bs.

Unit 1 (800–677 cm bs) is composed of four thin layers of sandy to silty sediments varying in color (Fig. 5). Brown sediments at 747–725 cm bs are normally graded, with texture gradually changing from coarse sand with few medium pebbles ($\varnothing < 3 \text{ cm}$, angular to subrounded) at the bottom to silty sand at the top. The uppermost layer (725–677 cm bs) consists of brown to yellowish-gray sandy silt with few weathered carbonate concretions. The yellowish-gray color of the sediment likely results from the weathered carbonate. At 770–725 cm bs, sediments are strongly calcareous. The graphs of measured bulk parameters have comparable trends with a slight decrease of pH, EC, and LOI_{550} values occurring around 770 cm bs. The Ca/Ti ratio has a median value of 17.75 (4.2, $n=10$) and a peak of 21 at the top of this unit (around 673 cm bs). The ratio of Zr/Rb has a median value of 1.45 (0.2, $n=10$). The boundaries among the

layers in this unit are gradual, and unit 1 sharply transitions to unit 2.

Unit 2 (677–427 cm bs) is characterized by poorly compacted, blackish-grayish clayey silt. Color varies slightly between dark greenish gray (Gley 1 3/5GY, 600–500 cm bs) and very dark gray (Gley 1 3/N, 500–436 cm bs). The sediments are moderately calcareous at 657–628 cm bs and slightly calcareous at 600–436 cm bs. Other than a single carbonate nest around 585 cm bs and few carbonate concretions at 677–657 cm bs, very few carbonate concretions occur in this unit. Sediments at 677–657 cm bs are clayey sandy silt, slightly coarser than the upper part (657–436 cm bs). The latter is characterized by a very strong emanation of an H_2S smell after adding 9.9% HCl, indicating the presence of Fe sulfides under reducing conditions (Jahn et al., 2006). At 436–427 cm bs, sediments are moderately calcareous, poor in clay content, and contain very few fine reddish iron mottles.

The pH values ($n=20$) gradually decrease from 8.5 (strongly alkaline) at the base to 8.2 (moderately alkaline) at the top. EC values ($n=20$) gradually increase from ca. 300 $\mu\text{S}/\text{cm}$ (class 2) at the bottom to 500 $\mu\text{S}/\text{cm}$ (class 3) at the top. X_{LF} values remain low ($35 (3) \times 10^{-8} \text{ m}^3/\text{kg}$, class 2, $n=14$) at 600–440 cm bs, where LOI_{550} values reach the maximum (6.7 (0.5) mass%, class 5, $n=20$) of the whole profile. Element ratios of Ca/Ti (8.65 (2.0), $n=20$) and Zr/Rb (0.94 (0.1), $n=20$) remain low. Two organic-rich bulk samples from 665 cm bs and 460 cm bs date to 6187–5947 cal yr BP and 4959–4833 cal yr BP, respectively. The sediment boundary between units 2 and 3 is sharp.

Unit 3 (427–320 cm bs) shows slightly calcareous and normally graded sediments. The texture gradually changes from light olive brown (2.5 Y 5/3) pebbly coarse sand at the base, to medium-coarse sand in the middle, to dark yellowish-brown (10YR 4/6) fine sand at the top. Very few manganese mottles and few micas occur in the upper part of the unit (320–315 cm bs). Sediments are strongly alkaline (pH: 8.7 (0.1), $n=5$). Median values ($n=5$) of EC (112 (11) $\mu\text{S}/\text{cm}$, class 1) and LOI_{550} (0.8 (0.1) mass%, class 1) are the lowest of the whole profile. X_{LF} values ($114 (19) \times 10^{-8} \text{ m}^3/\text{kg}$, class 4, $n=5$) peak at ca. 400 cm bs ($143 \times 10^{-8} \text{ m}^3/\text{kg}$, class 5) and gradually decrease to $80 \times 10^{-8} \text{ m}^3/\text{kg}$ (class 3) at the top. Ca/Ti values (14.68 (2.0), $n=5$) are slightly higher than in unit 2. The Zr/Rb ratio peaks around 400 cm bs (3.91) and decreases toward the top. The boundary between unit 3 and the overlying unit 4 is sharp.

Unit 4 (320–224 cm bs) continues the trend of decreasing grain size with decreasing depth. The moderately calcareous sediments consist of brown (7.5 YR 5/4) coarse sand at the bottom, sandy silt at the middle, and dark reddish-gray (5 YR 4/2) sandy clayey silt at the top. Weathered fragments of carbonate rocks occur at 239–232 cm bs and very few manganese mottles at 244–224 cm bs. Sediments are strongly alkaline (pH: 8.5 (0.1), $n=6$). EC values gradually increase from 140 $\mu\text{S}/\text{cm}$ (class 1) at the base to 487 $\mu\text{S}/\text{cm}$ (class 3) at the top. Median X_{LF} values ($106 (7) \times 10^{-8} \text{ m}^3/\text{kg}$, class 4, $n=6$) remain in the same range as in the underlying unit 3. Also, the LOI_{550} median value is around 1.5 (0.7) mass% (class 1, $n=6$) and shows the same range as in unit 3. The Ca/Ti ratio (12.63 (1.9), $n=6$) and Zr/Rb ratio (1.40 (0.1), $n=6$) exhibit a slight increase from the bottom to the top and display small peaks in the upper part. The boundary with overlying unit 5 is gradual.

Unit 5 (224–107 cm bs) shows reddish-brown (5 YR 4/4), strongly compacted clayey silt with very few embedded fine pebbles. Manganese mottles commonly exist in this unit with slightly decreasing abundance from the bottom to the top.

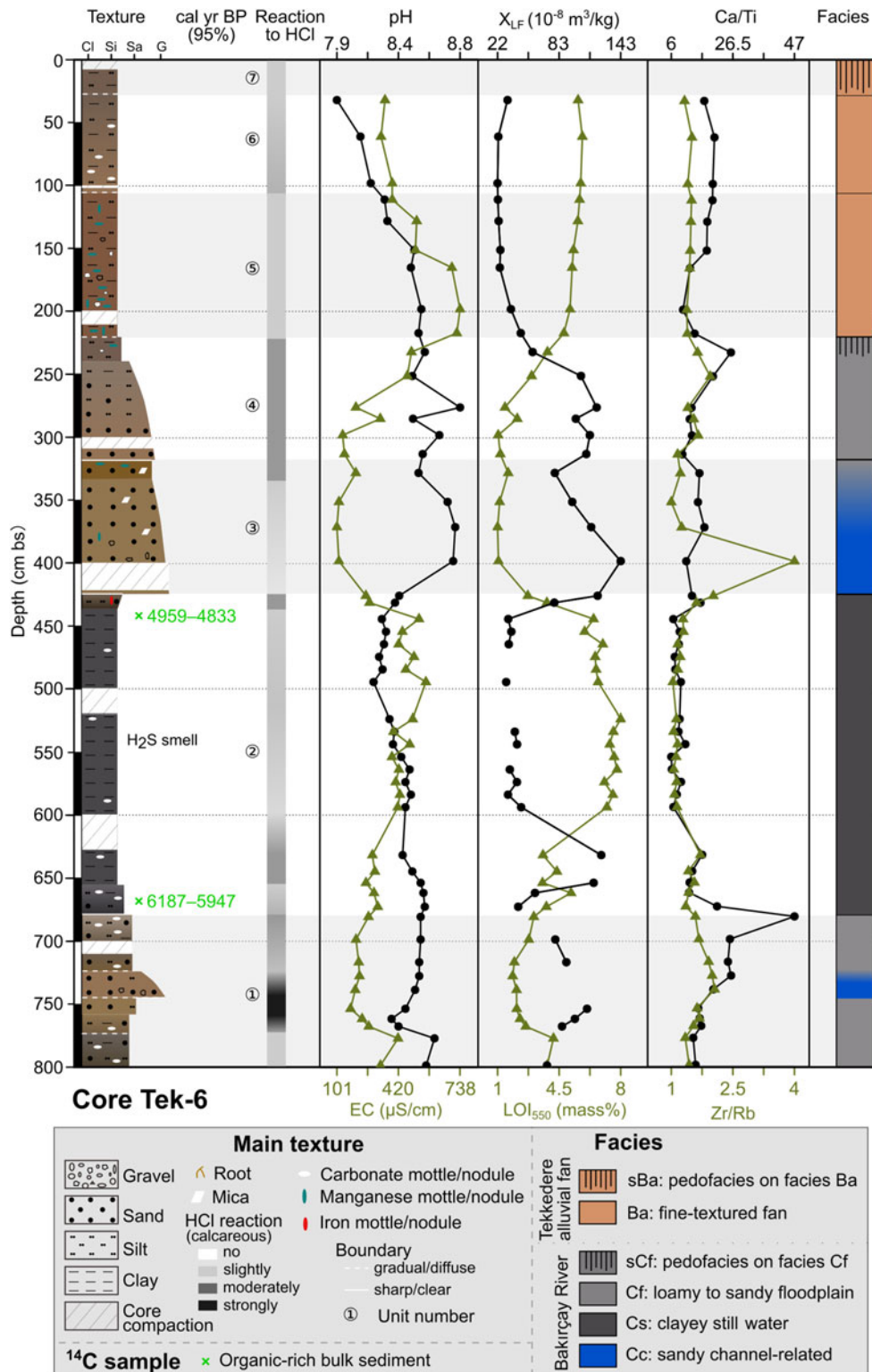


Figure 5. The lithostratigraphy, radiocarbon dates, and sediment analyses of sediment core Tek-6. cm bs, cm below surface; EC, electrical conductivity; LOI₅₅₀, loss on ignition at 550°C; X_{LF} , mass-specific susceptibility at the low frequency.

Sediments are slightly calcareous and very few fine to medium carbonate fragments occur at 200–150 cm bs. The boundary with overlying unit 6 is a gradual contact.

Unit 6 (107–29 cm bs) consists of brown (7.5 YR 5/4), slightly calcareous clayey silt. The compactness and carbonate content

decrease with decreasing depth. Sediments from units 5 and 6 are moderately alkaline with decreasing pH values from the bottom to the top. EC values gradually decrease from ca. 730 μ S/cm (class 5) in unit 4 to 330 μ S/cm (class 2) in unit 6. Median X_{LF} values in units 5 and 6 are low without remarkable

oscillations ($24 (1) \times 10^{-8} \text{ m}^3/\text{kg}$, class 1, $n = 9$). LOI_{550} values in both units are relatively high (5.2 (0.2) mass%, class 4, $n = 9$) compared with the underlying units 3 and 4 (1.1 (0.4) mass%, class 1, $n = 11$). The Ca/Ti ratio (17.58 (1.7), $n = 9$) is high and the Zr/Rb ratio (1.22 (0.1), $n = 9$) is low in units 5 and 6. Unit 6 gradually transitions to unit 7.

Unit 7 (29–0 cm bs) corresponds to the present-day plow horizon, which consists of brown (7.5 YR 4/2), heavily compacted clayey silt.

SEDIMENT FACIES

Similar to previous studies in the Pergamon micro-region (Schneider et al., 2014, 2015), sediment facies in the eight Tekkedere profiles are identified based on their geomorphological setting, field observation, sediment texture, and measured sediment characteristics (Blair and McPherson, 1994; Brown, 1997; Goldberg and Macphail, 2006; Miall, 2006, 2014).

Facies A: Tekkedere valley bottom sediments

Sediments that filled the Tekkedere valley, that is, profiles Tek-1 (Supplementary Fig. 2), Tek-2 (Fig. 3), and Tek-3 (Supplementary Fig. 3), are classified as facies A (Tekkedere valley bottom sediments). Facies A is further subdivided into fine-textured (facies Aa) and coarse-textured (facies Ab) deposits (Table 4). They were predominantly deposited by fluvial processes of the Tekkedere creek (Fig. 2A and C), as evidenced by the sediment lithology and topographical location (Goldberg and Macphail, 2006). Fluvial sediments are partly interfingering with colluvial deposits characterized by massive bedding and poor sorting (Mills, 1979; Brown, 1997; Miall, 2014). The development of fine- and coarse-textured valley bottom sediments in Tekkedere is different from the formation of sediments in the Gümüş valley, where fine-grained sediments dominate (Knitter, 2013).

Facies Aa (fine-textured sediments) contains lower coarse fraction content (grains $< 2 \text{ mm}$ are less than 10%), whereas facies Ab (coarse-textured) shows distinctively higher coarse fraction content (reaching 60%) (Fig. 3). Compared with facies Aa, facies Ab is mostly more alkaline and shows lower EC and LOI_{550} values. Parts of the fine-textured sediments present typical post-sedimentary and pedogenic features, including common animal burrows and roots, relatively dark color, low pH, high EC, and increased LOI_{550} values. They document processes of humification and consequently are classified as buried topsoil horizons (pedofacies sAa in Table 4; Goldberg and Macphail, 2006), such as the buried soil horizon of unit 4 in Tek-2 (Fig. 3). This facies indicates a poorly developed soil horizon, pointing to a short period of reduced land erosion activity (Dusar et al., 2011).

Facies B: Tekkedere alluvial fan sediments

The deposition of the Tekkedere alluvial fan is predominantly formed by brownish fan sediments (facies B). Facies B is also differentiated into fine-textured (facies Ba) and coarse-textured (facies Bb) deposits (Table 4) with distinct characteristics of alluvial fan deposits (Blair and McPherson, 2009; Bowman, 2019). Facies Ba is inferred from the generally fine composition of grain size (clayey to silty sediments with a low proportion of pebbles), often increased EC and LOI_{550} values, and very low results for X_{LF} values and Ca/Ti and Zr/Rb ratios. In contrast, facies Bb

Table 4. The features of different sediment facies in the Tekkedere catchment.

Facies	Description ^a	
Tekkedere valley bottom sediments (A)	Aa	Fine-textured valley bottom sediments, containing less than 10% coarse fraction ($> 2 \text{ mm}$)
	sAa	Buried topsoil horizons on the fine-textured valley bottom sediments (facies Aa) with high bioturbation and higher EC and LOI_{550} values compared with facies Aa
	Ab	Coarse-textured valley bottom sediments, with coarse fraction contents in the range of 10–60%; mostly more alkaline; decreased EC and LOI_{550} values
Tekkedere alluvial fan sediments (B)	Ba	Fine-textured alluvial fan sediments, characterized by clayey to silty sediments with a low portion of pebbles; often increased EC and LOI_{550} values; low X_{LF} and element ratios of Ca/Ti and Zr/Rb
	sBa	Buried topsoil horizons on the fine-textured alluvial fan sediments (facies Ba), with a distinct increase in LOI_{550} values compared with facies Ba
	Bb	Coarse-textured alluvial fan sediments, containing more coarse components (mainly sands with fine to medium pebbles) with less Fe–Mn mottles; very low EC and LOI_{550} values; increased X_{LF} and element ratios of Ca/Ti and Zr/Rb
Bakırçay River sediments (C)	Cc	Channel-related sediments of the Bakırçay River, containing fining upward pebbly sand with remarkably low LOI_{550} values and relatively high Zr/Rb ratio
	Cf	Floodplain sediments of the Bakırçay River, dominated by sandy silt; compared with the Tekkedere alluvial fan sediments (facies B), generally higher LOI_{550} and EC values, but lower X_{LF} and element ratios of Ca/Ti and Zr/Rb
	sCf	Buried topsoil horizons on the Bakırçay floodplain sediments (facies Cf), with increased LOI_{550} values compared with facies Cf
	Cs	Still water sediments of a poorly drained environment on the Bakırçay floodplain, containing dark gray silty clay with very high LOI_{550} values; strong H_2S smell after adding 9.9% HCl

^aEC, electrical conductivity; LOI_{550} , loss on ignition at 550°C; X_{LF} , mass-specific susceptibility at the low frequency.

contains more coarse components (sands with fine to medium pebbles) and fewer Fe–Mn mottles than facies Ba, for example, unit 1 in Tek-4 (Supplementary Fig. 4) and units 5 and 7 in Tek-5 (Fig. 4). Facies Bb usually shows very low EC and LOI_{550} values, but increased X_{LF} and element ratios.

Following the alluvial fan's longitudinal profile (the transect from the fan apex to its toe; Fig. 6), two major cycles of fine- and coarse-textured fan sediments can be identified in the mid-fan position, that is, profiles Tek-5 and Tek-4-2. In general, the

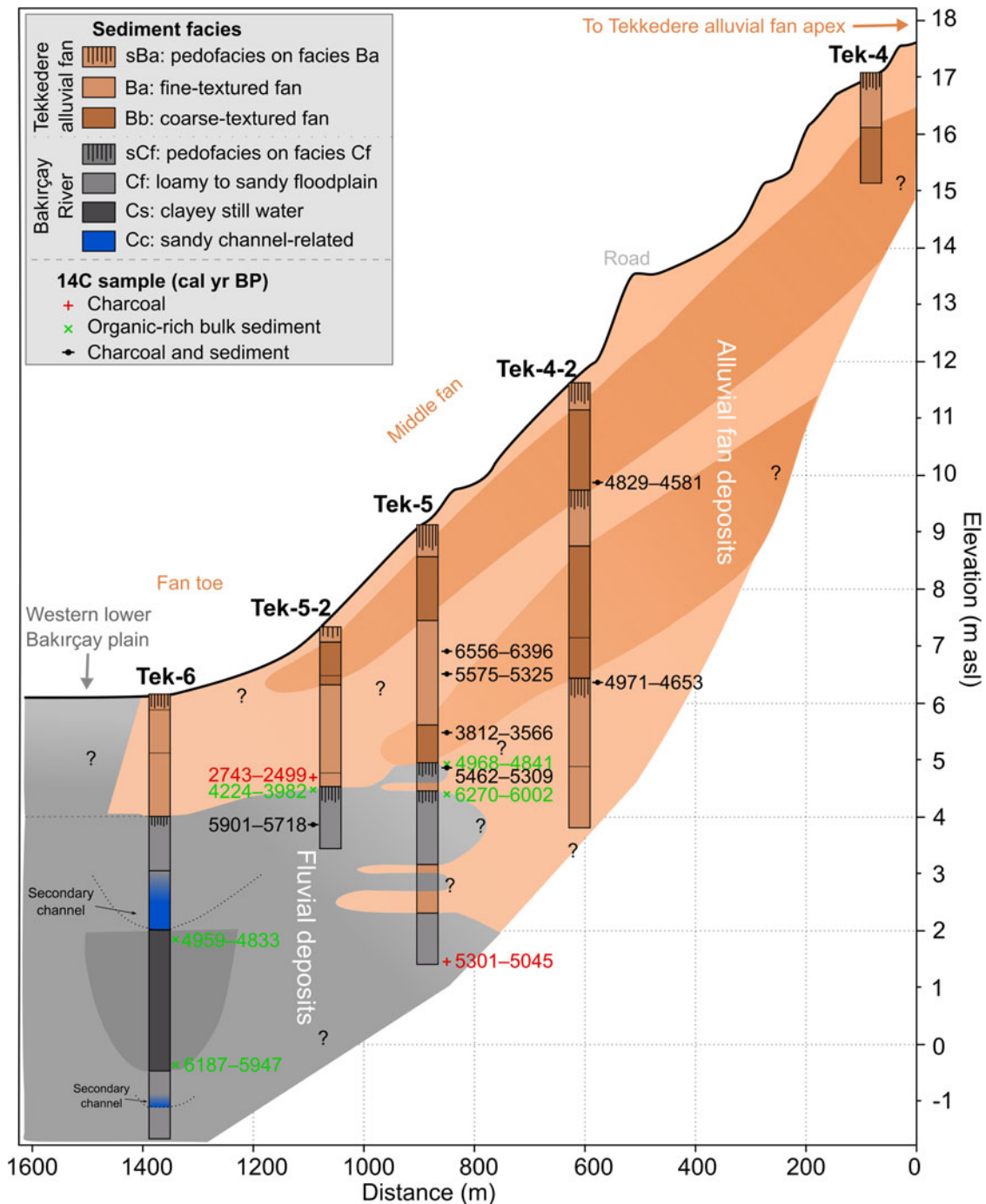


Figure 6. Longitudinal profile along with the Tekkedere alluvial fan (91 × vertical exaggerations) with sediment cores. Display of the thickness of the different units corresponds to height scale, and sediment architectures are based on the sediment units of the different cores. Embedded calibrated radiocarbon ages provide an overview of sediment ages and age inversions. m asl, m above sea level.

texture of facies Ba and Bb fines from the apex to the toe of the alluvial fan, and the thickness of layers declines in parallel (Fig. 6), which is also reported on the alluvial fans in western Turkey (Özpolat et al., 2020). In addition, the thin layers of facies Ba, which only vertically discontinuously occur in the lower part of Tek-5, can be linked with the fine-textured sediments below 463 cm bs in Tek-4-2 (Fig. 6).

Increased LOI₅₅₀ values in units 2 and 5 of Tek-4-2 (Supplementary Fig. 5) indicate the evidence of buried topsoil

horizons developed on the fine-textured alluvial fan deposits, reaching a thickness up to 30 cm (facies sBa in Fig. 6 and Table 4; Soil Survey Staff, 1999; Kapur et al., 2017; Macphail and Goldberg, 2017).

Facies C: Bakırçay River sediments

Given that the position of the fan toe is proximal to the Bakırçay River, the dark-colored and organic-rich sediments in the lower part of the profiles extracted at the middle-distal part of the fan

(profiles Tek-5, Tek-5-2, and Tek-6) are interpreted as Bakırçay River deposits (facies C in Fig. 6; cf. Goldberg and Macphail, 2006; Miall, 2006). Most of these sediments correspond to sandy silts, whereas coarse sands and angular pebbles are nearly absent. The Ca/Ti ratio in facies C is generally lower than in facies B, likely associated with the differences in the occurrence and distribution of carbonate rocks in the drainage basins of Bakırçay and Tekkedere (MTA, 2002; Yang et al., 2021; Fig. 2B).

Field observation in the present-day Bakırçay floodplain indicates subenvironments of the abandoned channel, paleo-oxbow, and over-bank, which are comparable to those of the Büyük Menderes floodplain in western Turkey (Özpolat et al., 2020). Based on sediment characters and their occurrence in proximity to the present-day floodplain, the sandy-silty sediments are interpreted as Bakırçay River floodplain deposits (facies Cf in Table 4; cf. Miall, 2006). These floodplain deposits can be observed in units 1 and 3 of Tek-5 (Fig. 4), unit 1 of Tek-5-2 (Supplementary Fig. 6), and units 1 and 4 of Tek-6 (Fig. 5). In the lower part of profile Tek-5 (mid-fan position), the floodplain deposits (facies Cf) interfingered with layers of fine-textured alluvial fan sediments (facies Ba), that is, units 2 and 4 in Tek-5 (Figs. 4 and 6). None of the alluvial fan sediments (facies B) occur in the lower parts of Tek-5-2 and Tek-6 (the toe of the Tekkedere fan).

The 2.5-m-thick unit of dark gray silty clay with very high LOI_{550} values (unit 2 in Tek-6; Fig. 5) is interpreted as still water sediments (facies Cs; Table 4) of an oxbow lake or a (secondary) channel (Miall, 2006, 2014; Charlton, 2007). Sediments overlying facies Cs in Tek-6 show a distinct fining-upward feature, from pebbly sand (unit 3) to sandy silt (unit 4) (Fig. 5). This gradual change in grain size reflects a reduction in the sediment transportation ability of the Bakırçay River. The decreasing fluvial activity points out a high-energy channel-related environment (facies Cc) transferred to a low-energy floodplain (facies Cf) (Miall, 2006). In the middle part of unit 1 in Tek-6, a similar feature of abandoned channel-related deposits (facies Cc) can be observed, but it is less thick and distinct (Fig. 6). In general, the gradual change in vertical lithostratigraphy indicates a meandering pattern (Miall, 2006). This is supported by Aksu et al. (1987) who suggest a strongly meandering channel pattern of the Bakırçay in its lower course during the Late Quaternary.

Redoximorphic features of Mn–Fe nodules as well as secondary precipitated carbonates prevailing in the Bakırçay floodplain deposits reflect the effect of a post-sedimentary seasonally fluctuating groundwater table (Goldberg and Macphail, 2006). These postdepositional processes have also been reported in several locations in the lower Bakırçay basin (Schneider et al., 2014, 2015, 2017).

Boundaries between the facies of the Bakırçay River floodplain (facies Cf) and the overlying facies of the Tekkedere alluvial fan (facies B) in profiles Tek-5, Tek-5-2, and Tek-6 are roughly at the same absolute elevation (ca. 4–5 m asl; Fig. 6). At these boundaries, the floodplain deposits frequently show weakly developed thin fossil soil horizons (facies sCf; Fig. 6, Table 4), that is, the buried paleosols in the upper part of units 3 and 4 in Tek-5 (Fig. 4), unit 1 in Tek-5-2 (Supplementary Fig. 6), and unit 4 in Tek-6 (Fig. 5). Comparable to soil facies sAa in the Tekkedere valley bottom, this pedofacies sCf with its immature A horizon documents past soil formation and a stable surface on the floodplain.

MID- TO LATE HOLOCENE GEOMORPHODYNAMICS

The lithostratigraphic analyses and the radiocarbon ages indicate four major geomorphodynamic phases from the Middle to Late Holocene (Figs. 6 and 7).

Phase 1 (ca. 6.2 to 5–4 ka): aggradation of the Bakırçay floodplain

Sediment dynamics during the first phase are mainly related to the deposition of Bakırçay River sediments (facies C), for example, the floodplain aggradation. Proximal to the current Bakırçay channel, the paleo-floodplain (facies Cf) at the Tek-6 location was first dissected by a (secondary) channel (facies Cc) (Fig. 6). The channel was then filled by sediments with the fining upward feature. Hereafter, a still water environment (facies Cs) existed for more than a millennium (from 6.1 to 4.9 ka; Table 3). It was then dissected by a younger channel (facies Cc) and successively covered with silty floodplain deposits (facies Cf). The upper floodplain layers (facies Cf) in profile Tek-6 are linked to the floodplain sediments in Tek-5-2 based on the same absolute elevation at ca. 4–5 m asl (Fig. 6). More distal to the current Bakırçay River, floodplain deposits (facies Cf) in Tek-5 interfinger with the sediments originating from the Tekkedere catchment (facies Ba), which indicates the location of Tek-5 marks a former overlapping zone of the peripheral Bakırçay plain and the Tekkedere fan.

The beginning of the Bakırçay floodplain aggradation in the area of the present-day Tekkedere fan predates ca. 6.2 ka. This is revealed by the radiocarbon sample from the bottom of the still water sediment in Tek-6 (6187–5947 cal yr BP at 665 cm bs; Table 3). Accordingly, the underlying floodplain (facies Cf) and the secondary channel (facies Cc) deposits were older than 6.2 cal ka BP. The Bakırçay floodplain sediments continued to deposit in the distal part of the current Tekkedere alluvial fan at least until 5301–5045 cal yr BP, which is indicated by the charcoal sample at 781 cm bs in Tek-5 (Table 3). Although it has to be considered that radiocarbon dates of charcoals are often interpreted as the maximum depositional age due to the possible reworking of the samples before their last deposition (Lang and Hönscheidt, 1999; Chiverrell et al., 2007; Nykamp et al., 2020), the aforementioned charcoal, because of its considerable size (\varnothing = ca. 0.5 cm, larger than other charcoal pieces) and its deposition in fine floodplain sediments, is considered to have been deposited a rather short time after being burned. Hence, it is acceptable to use the charcoal date as the depositional age of the surrounding sediments.

The termination of floodplain aggradation in the first phase is marked by the formation of soil horizons (Fig. 6). The dating of the end of phase 1 is precarious due to several age inversions and the specific characteristics of different dated materials. In Tek-5, the dating results of the two samples from 478 cm bs (6270–6002 cal yr BP) and 435 cm bs (5462–5309 cal yr BP) are most likely overestimated (Fig. 6), because the charcoal sample taken from the bottom of the profile (781 cm bs, 5301–5045 cal yr BP) represents a maximum depositional age of the overlying deposits. We therefore suggest the dating samples from the soil horizons (around 430 cm bs in Tek-5) incorporated older materials, such as reworked and washed terrestrial soils and organics (Fowler et al., 1986; Strunk et al., 2020). However, an alternative interpretation of dating results from bulk soil samples is possible. Based on the open system of soil formation (Scharpenseel and Schiffmann, 1977; Wang et al., 1996; Kovda et al., 2001), radiocarbon ages of organic-rich bulk samples are considered to be minimum ages since the initiation of soil formations (Scharpenseel and Schiffmann, 1977; Wang et al., 1996). In this sense, the time of the soil formation and the deposition of the parent material should be even older than the dating result of the bulk sample

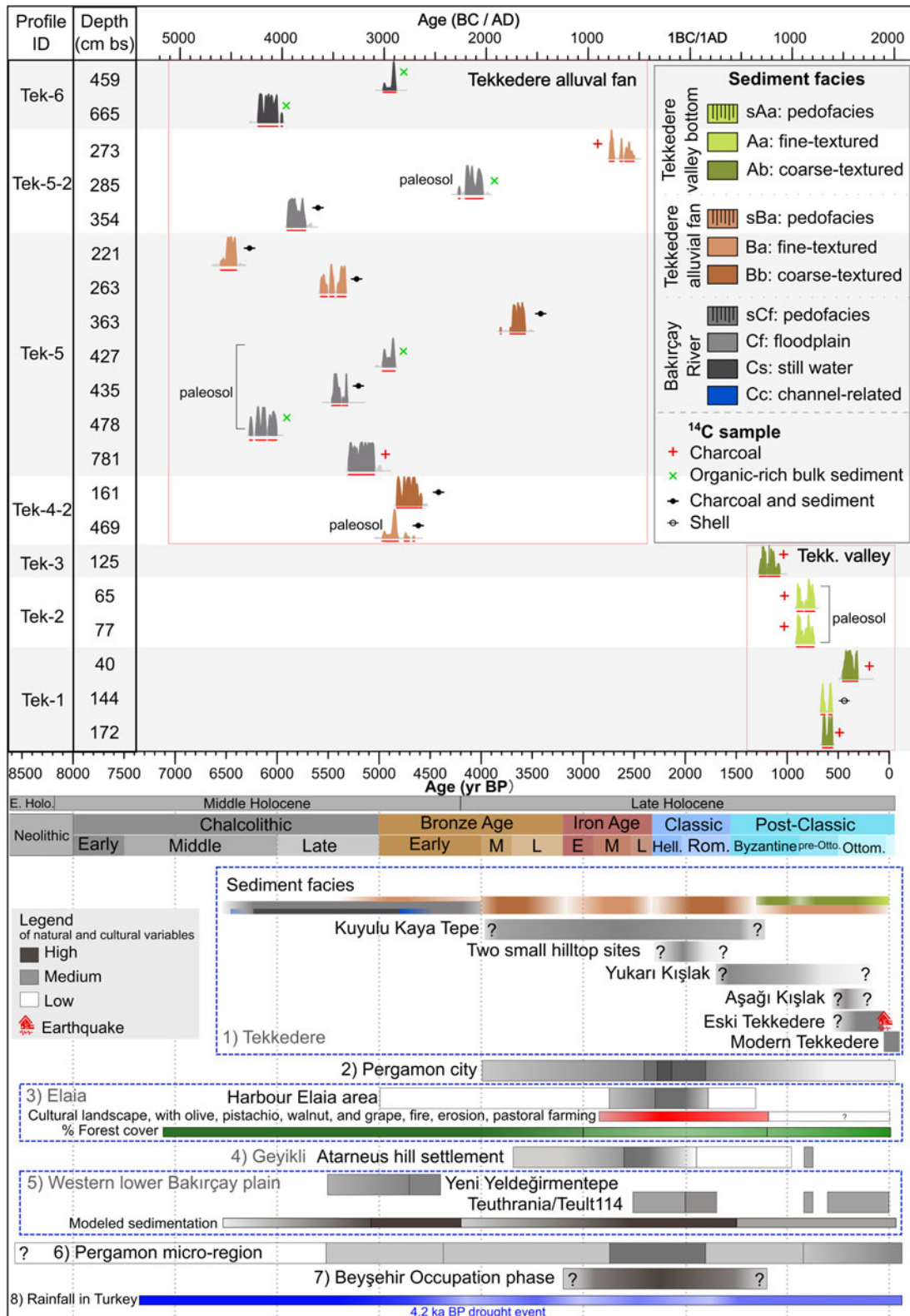


Figure 7. The calibrated radiocarbon ages of the samples from the Tekkedere area and the natural and cultural variables in the Pergamon micro-region. Data set: 1) Tekkedere: sediment facies (this study) and preliminary results of the human occupation (Ludwig, 2020a; Michalski, 2021; Tozan, 2022) and earthquake in 1939 (Paradisopoulou et al., 2010; Çelik et al., 2019; Pirson, 2020; Tozan, 2022); 2) preliminary results of occupation in Pergamon city (Pirson, 2017); 3) Elaia: preliminary results of occupation (Pirson, 2014; Pirson et al., 2015; Feuser et al., 2020) and landscape and forest cover (Shumilovskikh et al., 2016; Seeliger et al., 2019); 4) Geyikli: preliminary results of occupation in Atarneus hill settlement (Schneider et al., 2013, 2014; Zimmermann et al., 2015); 5) western lower Bakırçay plain: preliminary results of occupation in Yeni Yeldeğirmen-tepe (Horejs, 2010b, 2011b; Schneider et al., 2017) and Teuthrania/Teult114 (Schneider et al., 2015; Williamson, 2016) and modeled sedimentation (Becker et al., 2020a); 6) preliminary results of occupation in the Pergamon micro-region (only valid for its western part) (Horejs, 2010a, 2011a, 2014; Pirson and Zimmermann, 2014); 7) Beyşehir Occupation phase (Eastwood et al., 1998); 8) rainfall in Turkey (Finné et al., 2019). Abbreviations: E, Early; M, Middle; L, Late; Hell., Hellenistic Period; Rom., Roman Imperial Period; pre-Otto., pre-Ottoman; Ottom., Ottoman.

at 478 cm bs of Tek-5 (6270–6002 cal yr BP). Nonetheless, this is inconsistent with the charcoal dating result.

The date of the bulk sample at 427 cm bs (4968–4841 cal yr BP) in Tek-5 (Fig. 6) indicates soil formation continued after ca. 5.0 ka. The bulk sample from the buried surface of the floodplain (facies sCf, 4224–3982 cal yr BP at 285 cm bs) in Tek-5-2 suggests the floodplain aggradation occurred before 4 ka. In Tek-6, the uppermost layer of still water sediments dated to 4959–4833 cal yr BP represents the maximum burial age of the floodplain at this location. Thus, based on the dating results from the three profiles, the depositional termination of the Bakırçay River sediments in the area of the recent Tekkedere fan started before ca. 6.2 ka and ended between ca. 5 and 4 ka. Concurrently, the fine-textured Tekkedere alluvial fan deposits (facies Ba) accumulated at least to the location of Tek-4-2 and interfingering with Bakırçay River sediments at the location of Tek-5.

The dominant deposition of Bakırçay River sediments over Tekkedere fan deposits was mainly controlled by supraregional factors. It is assumed that the extensive aggradation of the Bakırçay River is associated with the rising sea level around the Elaiia Bay in the Aegean part of Turkey that slightly slowed down but continued after 6 ka (Kayan, 1999; Seeliger et al., 2017, 2019), resulting in the rise of the erosional base level (Robustelli et al., 2009). In addition, during the Middle Holocene, the prevailing wetter-than-today humid climate in Anatolia and the Balkans (Eastwood et al., 2007; Finné et al., 2019; Fig. 7, rainfall in Turkey) fostered fluvial dynamics (Walsh et al., 2019). Evidence for the increased sediment load and discharge of the Bakırçay River in the Tekkedere area (i.e., maximum floodplain extension, a 1000-year-long still water environment, and shifted secondary channels) coincides with this Middle Holocene humid period. These fluvial dynamics are not only observed in Tekkedere but also in other areas in the Pergamon micro-region (Schneider et al., 2015, 2017; Becker et al., 2020a) and the eastern Mediterranean region (Dusar et al., 2011; Benito et al., 2015; Glais et al., 2017; Bulkan et al., 2018; Ocakoğlu et al., 2019).

Simultaneously, we could assume that under the Middle Holocene humid climate and high forest cover (Shumilovskikh et al., 2016; Fig. 7), erosion sensitivity and sediment dynamics were low, which explains the middle Tekkedere alluvial fan (Tek-4-2 and Tek-5) during this phase only consisted of fine-textured sediments and had a low spatial extent (Fig. 6). The interfingering layers of floodplain and alluvial fan deposits in profile Tek-5 are attributed to torrential runoff events in the Tekkedere valley, possibly corresponding to short-term relatively arid events, as also recorded in Anatolia, for example, at Gediz Graben during 5.7–4.2 ka (Bulkan et al., 2018), the Kureyşler area at ca. 7.0–5.3 ka (Ocakoğlu et al., 2019), and Tecer Lake at ca. 5.3–5 ka (Kuzucuoğlu et al., 2011).

Human impacts on geomorphodynamics in the Tekkedere drainage basin during phase 1 might be negligible. Settlements may have existed in the Pergamon micro-region since the Neolithic, for example, Yeni Yeldeğirmen-tepe (Schneider et al., 2017) and many sites in the western lower Bakırçay catchment (Horejs, 2010a, 2011a, 2014; Pirson and Zimmermann, 2014; Pirson, 2022), but there was likely no occupation or land use in Tekkedere during this time (Michalski, 2021; Fig. 7).

Phase 2 (between ca. 5 and 4 ka): formation of floodplain soils

In all three sediment profiles where Bakırçay River sediments were extracted, that is, Tek-5, Tek-5-2, and Tek-6, organic-rich

topsoil horizons (facies sCf) developed on the floodplain deposits (facies Cf) (Fig. 6). The formation of the floodplain soil horizons is marked as the second phase of geomorphodynamics, which indicates no or negligible accumulation of materials and thus a phase of relative stability. Phase 2 is suggested to have occurred between ca. 5 and 4 cal ka BP, as dated by the bulk samples at 427 cm bs (4968–4841 cal yr BP) in Tek-5 and 285 cm bs (4224–3982 cal yr BP) in Tek-5-2 (Fig. 6).

Reduced flooding activities, as well as low accumulation of fan sediments, are the direct reasons for the soil formation, similar to the case study in the Central Ebro Basin (NE Spain) (Pérez-Lambán et al., 2018) and in the wider Mediterranean region (Collins et al., 2005; Vött et al., 2006; Dusar et al., 2011). The trend to floodplain stabilization or slow aggradation is in accordance with climatic drying since 5.2 ka, particularly when drier conditions dominated after 4500 yr BP (Finné et al., 2019). The climatic erosion sensitivity, hence, became relatively low (Dusar et al., 2011). In addition, the human disturbance in the Tekkedere catchment and the immediate vicinity might also be negligible in the second phase (Fig. 7), which altogether, promotes the development of the soil horizons.

Phase 3 (ca. 4–3.8 ka): transition from floodplain to fan environment and the onset of human impacts

The third depositional phase is characterized by the predominant deposition on the Tekkedere alluvial fan (facies B) that covered the floodplain soils (facies sCf; phase 2) and a terminal accumulation of the Bakırçay floodplain (facies C; phase 1). The mixed charcoal/sediment sample (3812–3566 cal yr BP, 363 cm bs) from the alluvial fan deposit overlying the buried soil in Tek-5 suggests the maximum depositional age of the fan sediment at this location (Fig. 6). Therefore, the transition from the floodplain (and floodplain soils) environment to the Tekkedere alluvial fan (presumably) took place between ca. 4 and 3.8 cal ka BP. The charcoal sample taken from the overlying fan sediments dates much later (2743–2499 cal yr BP, 273 cm bs) in Tek-5-2 which reveals a younger coverage of fan sediments at the distal location.

This remarkable transition corresponds to the Mid-/Late Holocene boundary and marks a substantial geomorphodynamic change in the area. Factors that trigger this transition from phases 1 and 2 to phase 3 likely include (1) the 4.2 ka BP drought event (Bini et al., 2019; Finné et al., 2019); (2) the onset of settlement activities in the catchment area (Ludwig, 2020a; Michalski, 2021; Fig. 7); and (3) the internal behavior of the fluvial system (Schumm, 1977), for example, the (secondary) channels of the Bakırçay River shifted to the west.

The 4.2 ka BP drought event, generally corresponding to the period from 4.3 to 3.8 ka BP, shows drier conditions throughout the Mediterranean winters, in addition to already dry summers (Bini et al., 2019). Because of its global significance, it defines a formal boundary between the Mid- and Late Holocene (Walker et al., 2019). More studies suggest this climate oscillation is not just one single dry event, but a highly dynamic succession of dry and wet events (Bini et al., 2019) affecting the worldwide development of seasonal rainfalls, vegetation cover change (Shumilovskikh et al., 2016; Di Rita et al., 2022), and ensuing torrential runoff and high-frequency environmental instabilities (Türkeş and Erlat, 2005; Kuzucuoğlu et al., 2011; Dreibrodt et al., 2014; Ocakoğlu et al., 2019; Lawrence et al., 2021). The change from dominating floodplain aggradation to enlarged fan

development as observed in Tekkedere, therefore, probably corresponds to the global effect of the 4.2 ka drought event.

In addition to a general change in climate, after the onset of the Late Holocene, human activities started at the Kuyulu Kaya Tepe in the Tekkedere valley (Ludwig, 2020a; Michalski, 2021; Figs. 2A and 7). The subsequent continuous occupation and agricultural and olive cultivation in the Tekkedere drainage basin (Ludwig, 2019, 2020a; Michalski, 2021; Tozan, 2022) accompanied by a generally dry climate caused the reduction of forest cover, as is evident from the past vegetation change in Elaia (Shumilovskikh et al., 2016; Fig. 7), which in turn accelerated the soil erosion processes and hillslope dynamics in the Tekkedere area.

In the Pergamon micro-region, the meta-analyses of previous studies suggest the modeled sediment facies and reconstructed geomorphodynamics in the western lower Bakırçay plain changed remarkably at ca. 4 ka, in relation to both triggers of climate change and continuous human settlements (Becker et al., 2020a). In Elaia, terrestrial input is for the first time observed to cover marine sediments after ca. 4 ka, which is associated with human-induced catchment erosion (Pint et al., 2015). An analogous environmental change is marked at 4.2 ka in Mediterranean France, where soil development was buried by rainfall-induced and ongoing human-exacerbated erosion (Brisset et al., 2013). In our study, it is still a challenge to distinguish the dominating trigger between the climate and humans on the increased geomorphodynamics during this period.

Notwithstanding the climatic drying and intensifying human activities on both Tekkedere and Bakırçay catchments, the important contribution of the Tekkedere alluvial fan sediments over the Bakırçay floodplains is assumed to be due to different landscape sensitivities (Yang et al., 2021), sediment (dis)connectivities, and reaction times (Goldberg and Macphail, 2006; Fryirs et al., 2007; Fryirs, 2013; Becker et al., 2020a). In addition, the internal shift in channel patterns is observed in the Bakırçay plain (Schneider et al., 2015; Becker et al., 2020b, 2022) and the Büyük Menderes plain (western Turkey) (Özpolat et al., 2020), which cannot be excluded for the location of the recent Tekkedere fan. However, no direct evidence is available.

Phase 4 (after ca. 3.8 ka BP): alluvial fan dynamics and changing human settlement pattern

During the ensuing Late Holocene, the geomorphodynamics in the Tekkedere catchment generally increased and varied spatio-temporally compared with the former phases. The increased geomorphodynamics are evident in the overall spatial enlargement of the alluvial fan coverage, the recurring coarse-textured fan deposits, age inversions (Fig. 6), and the lack of older valley bottom sediments. The alternating fine- and coarse-textured sediments (facies Ba and Bb) with occasionally developed soils (facies sBa) correspond to event layers and temporary landscape stability.

During the last phase, the alluvial fan sediments, particularly the coarse-textured materials, were for the first time deposited at the mid-toe part of the current alluvial fan (Fig. 6). This reveals that more sediments were produced at the unstable land surface and transported along the valley bottom. Radiocarbon dating results of the alluvial fan sediments (facies B) show several age inversions (Tek-5 and Tek-4-2; Fig. 6), reflecting the reworking of older deposits stored in temporal sinks due to the intensified sediment erosion in the catchment. This corresponds to the sediment cascade model (Lang and Hönscheidt, 1999), which has

been reported in other studies in the Mediterranean region (Vita-Finzi, 1969; van Andel et al., 1990; Nykamp et al., 2021; Cartelle et al., 2022).

A comparison of local, regional, and supraregional records indicates that a general trend of aridization, rapid climate change (RCC) events, and human activities were the major triggers for the Late Holocene changing geomorphodynamics (Constante et al., 2010; Duser et al., 2011, 2012; Shumilovskikh et al., 2016; Finné et al., 2019; Roberts et al., 2019a, 2019b; Becker et al., 2020a; Fig. 7). In general, the Late Holocene hydroclimate becomes drier than the Early–Mid-Holocene (Eastwood et al., 2007; Finné et al., 2019; Bozyiğit et al., 2022). It shows various fluctuations in different Mediterranean regions (Duser et al., 2011; Finné et al., 2019). Centennial-scale climate oscillations between aridity and humidity during the Late Holocene have been widely reported in Anatolia, where the Earth's surface responded to the rapid events accordingly both in coastal and hinterland areas (Kuzucuoğlu et al., 2011; Bulkan et al., 2018; Bassukas et al., 2021; Bozyiğit et al., 2022). A study in central Turkey indicates alternating humid (ca. 3.9–3.8, 3.65–3.55, 3.4–3.4 ka) and dry (3.8–3.65, 3.5–3.4, 3.25–3.0 ka) episodes, followed by an erosion crisis in 2.8–2 ka and a drying episode in the Roman climatic optimum (ca. 2–1.5 ka) (Kuzucuoğlu et al., 2011). In southwest Turkey, stable isotope analyses further suggest wetter conditions during Classical and Early Byzantine times (Eastwood et al., 2007). The climatic drying trend, amplified by the RCC events in the wider eastern Mediterranean region, presumably triggered the repetition of the sediment dynamics in the Tekkedere catchment.

Settlement activities in the Tekkedere valley continued from the hilltop of the Kuyulu Kaya Tepe since the late Middle Bronze Age (Michalski, 2021). The location of settlement sites changed to flatter areas in the lower valley (Ludwig, 2020a; Tozan, 2022; Figs. 2A and 7). Strategies for settlement occupation and drivers of settlement abandonment (or the changing settlement pattern) vary in different geographic locations and societies throughout time and are hence controlled by environmental and societal factors (Butzer, 2005, 2012; Boyer et al., 2006; McLeman, 2011). Environmental triggers encompass various types of natural hazards such as RCC events, (flash) floods, earthquakes, landslides, volcanic eruptions, and the ensuing geomorphodynamics (soil erosion and mass movements) (Black et al., 2011; Duser et al., 2011; Palmisano et al., 2021; Zhang et al., 2021; Kennett et al., 2022). This last factor might be important in the Tekkedere catchment.

The recurring cycles of increased geomorphodynamics during the Late Holocene were presumably triggered by past settlement locations around steep slopes in the mountainous part of the Tekkedere catchment (Fig. 2A). These settlement areas are geomorphologically sensitive to climate change and intensified land use. Hence, soil erosion and sediment dynamics may have occurred rapidly in the most sensitive areas, in particular, during the recent two millennia (Table 5). Conceivably, erosion on the land surface further results in unfavorable areas for agricultural, arboricultural, and settlement use. For this reason, a concomitant change to a more suitable settlement location, for example, the fertile and less landscape-sensitive Tekkedere valley bottom and Bakırçay floodplain, is understandable. The nearest analogous studies have been reported in Elaia (Pint et al., 2015; Seeliger et al., 2019) and suggest the harbor was abandoned in the Late Roman period due to progressive erosional processes and the resultant siltation.

Table 5. The summary of settlements and natural–social relationships in the Tekkedere valley.

Settlements	Chronology	Geomorphological position	Erosion sensitivity	Hazards/ sediment dynamics	View, traffic, agriculture accessibility
Kuyulu Kaya Tepe	Late Middle Bronze Age to the end of the Early Byzantine Period	Rock plateau and footslopes	Medium	Repeated high/low dynamics	Likely a fortress
Two small hilltop sites	Hellenistic Period to the Roman Imperial Period	Top of small hills	Medium-high	Likely high dynamics	Low
Yukarı Kışlak (upper settlement)	Late antiquity and likely to the Byzantine Period	Across the upper valley of creek B (valley bottom and slopes)	Medium	Likely from low to high dynamics	Low ↓ High
Aşağı Kışlak (lower settlement)	Unknown, likely between the occupation of Yukarı Kışlak and Eski Tekkedere	Northern slopes of the middle valley	High	Likely high dynamics	
Eski Tekkedere (old Tekkedere)	Before 1939	Northern slopes of the middle valley	High	Earthquake-triggered landslide	
Modern Tekkedere	Since 1939	Northern slopes of the lower valley	High	Unknown	

In addition to soil erosion, earthquakes would also be an important trigger for the shifting occupation of settlements in the Tekkedere catchment. In the Pergamon micro-region, at least nine earthquakes have been documented during the last two millennia (Nalbant et al., 1998; Emre et al., 2005; McHugh et al., 2006; Paradisopoulou et al., 2010; Schneider et al., 2014; Seeliger et al., 2017). Of particular note, the abandonment of the old Tekkedere settlement (Eski Tekkedere) and its relocation to the modern village took place due to the earthquake-triggered landslide in September–November 1939 (Paradisopoulou et al., 2010; Çelik et al., 2019; Fig. 7, Table 5).

In addition to the geomorphodynamics, rapid cold and dry climate events or heavy and unstable rainfall have been reported to cause settlement abandonment (Weiss, 2016; Bini et al., 2019). Due to flood threat, rural settlements in the Pergamon micro-region were built on elevated locations (Knitter, 2013; Schneider et al., 2015). In general, these extreme natural hazards led to relatively short-distance settlement relocation (Black et al., 2011), which explains the settlement mobility in Tekkedere.

Notwithstanding potential natural triggers, sociocultural factors also influenced settlement dynamics in Tekkedere. In the case of Kuyulu Kaya Tepe, political-administrative reasons in the Late Hellenistic–Early Roman Period (third to second centuries BC) probably led to the razing of the fortified rock plateau (Table 5). The demilitarization also happened in the neighboring hilltop settlements of Teuthrania and Eğrigöl Tepe (in the lower Bakırçay plain) and Atarneus (the Geyikli river area in Fig. 1; Schneider et al., 2014; Zimmermann et al., 2015; Williamson, 2016; Pirson, 2017; Ludwig, 2020a). The reasons for the final abandonment of the Kuyulu Kaya Tepe settlement in Byzantine times are obscure, and a combination of human impacts and changing environmental conditions may have played a role. The gradual settlement relocation towards the downstream of the Tekkedere valley may have been influenced by the accessibility of major traffic routes and agricultural areas (Table 5), although other studies have attributed settlement abandonment and migration solely to human causes such as military strategies and socio-cultural dynamics (Butzer, 2012; Schneider et al., 2014; Weiberg et al., 2019) or at most societal and environmental factors in combination (Black et al., 2011; Brown and Walsh, 2017).

Beyond Tekkedere, intensified sediment dynamics have been indicated from several alluvial fans and colluvium in the western lower Bakırçay plain since the Early Iron Age (Becker et al., 2020a; Fig. 7). Since then, large settlements such as Pergamon, Elaia, Teuthrania, Halisarna, and Atarneus gradually arose and the population increased (Pirson, 2008; Pirson and Zimmermann, 2014; Zimmermann et al., 2015; Pavúk and Horejs, 2018; Feuser et al., 2020; Fig. 7). Among them, the transformation of Pergamon from the Hellenistic Period to the Roman Imperial Period is of greatest significance (Pirson, 2020). To meet the increasing demand for cultivated crops and wood as food and construction materials (Kobes, 1999; Laabs and Knitter, 2021), Pergamon had remarkable impact on land use in rural areas, such as Tekkedere. Likewise, the ancient harbor cities (Elaia and Kane) and the monumental tumulus encountered human reshaping and construction of the land surface (Fediuk et al., 2019; Seeliger et al., 2019; Mecking et al., 2020).

Increasing landscape instability after land abandonment due to the concomitant absence of landscape management (cf. Schneider et al., 2014; Weiberg et al., 2021) is negligible for Tekkedere valley, because continuous human occupation is recorded here for roughly the last four millennia. The same reason may also apply to the difference in geomorphodynamics between the Tekkedere and Geyikli valleys. The depositional system in Geyikli is reported to have remained generally stable during the last 4000 years (Schneider et al., 2014), which is presumably related to the limited human impacts during ca. 2.3–1.9 ka BP (Schneider et al., 2013).

Throughout western Anatolia, particularly during the Beyşehir occupation phase (Classical and Early Byzantine times, ca. 3.2–1.3 ka BP; Kaniewski et al., 2007; Fig. 7), human impacts (forest clearance, fire activities, and grazing) have had a remarkable influence on the local landscape (Eastwood et al., 1998; Knipping et al., 2007; Dusar et al., 2011; Finné et al., 2011; Schneider et al., 2013; Stock et al., 2020). Likewise, continuous human activities since the Bronze Age (ca. 3.7 ka BP) may have strongly disturbed the landscape stability in Tekkedere and contributed to the ensuing colluviation, valley infill, and alluvial fan deposition in the western Yunt Dağı Mountains. The palynological archives from Elaia (Shumilovskikh et al., 2016), the olive cultivation (Tozan,

2022) accompanied by deforestation, and the occurrence of ceramic fragments in profile Tek-5 (Fig. 4) point to increased human activities in the Tekkedere catchment, though the duration and intensity of activities in different locations of the valley are currently unclear (Ludwig, 2020a; Michalski, 2021; Tozan, 2022; Fig. 7).

The infills of the Tekkedere valley bottom (facies A) date younger than ca. 1300 yr BP, which again reveals the removal of old materials by former increased geomorphodynamics was followed by ongoing sediment accumulation and a corresponding phase of increased erosion. The dynamics of fine- and coarse-textured sediments (facies Aa and Ab) and the local initial soil formation (facies sAa) in the Tekkedere valley bottom also suggest the erosion and stability repeated and varied spatiotemporally in the catchment during the last 1300 years. A similar process that resulted in substantial siltation is reported in Elaia, which continued during ca. 1.8–1.1 ka (Seeliger et al., 2013, 2019; Shumilovskikh et al., 2016). The onset of the modern trend toward aridity about 1300 years ago in southwest Turkey (Eastwood et al., 2007), the transition to the Little Ice Age (Kuzucuoğlu et al., 2011), and the various land use around the local settlements in Tekkedere (Fig. 7) together have the potential to have influenced the geomorphodynamics during the last millennium.

CONCLUSIONS

The geoarchaeological investigation of the Tekkedere alluvial fan and its catchment is the first detailed study that focuses on the Mid- to Late Holocene geomorphodynamics through alluvial sediments from a long-term settled valley in the hinterland of a major ancient city in western Turkey, the city of Pergamon. Sediment analyses, facies interpretation, and radiocarbon dating results suggest four principal phases of changing geomorphodynamics after 6.2 cal ka BP. In the first phase, before ca. 5–4 ka, the aggradation of the Bakırçay plain, that is, the deposition of still water sediments, channel beds, and floodplain sediments, dominated local geomorphodynamics. This period is generally characterized by rising sea level and the relatively humid Middle Holocene climate in western Anatolia. Alluvial soils that formed on the Bakırçay floodplain during phase 2 reflect a decline of the Bakırçay floodplain aggradation and low sediment dynamics in the Tekkedere catchment during a climatic phase of decreasing humidity between ca. 5 and 4 ka. The deposition of alluvial fan sediments from the Tekkedere valley was of low significance before ca. 4 ka. In the transition from the Middle to Late Holocene, the floodplain soils were buried by Tekkedere alluvial fan deposits (phase 3), pointing to the notably intensified geomorphodynamics in the Tekkedere catchment in comparison to the first two phases. This notable change is attributed to the supraregional trend of aridization and RCC events between 5 and 3 ka, superimposed by the onset of local human activities from the late Middle Bronze Age (ca. 3.7 ka) in the catchment. In the last phase, the indications of the enlarged fan coverage, the repetition of fine- and coarse-textured fan deposits, and the reworking of older sediments suggested by age inversions and young valley infills reveal increased geomorphodynamics during the Late Holocene. This increase is associated with the varying environmental conditions and natural hazards, soil erosion, and earthquake-triggered landslides, which largely affected local geomorphodynamics and consequent settlement activities.

A clear relationship between the climate variations, the changing settlement patterns, and geomorphodynamics, especially

during the Late Holocene, remains unclear due to several age inversions that make the timing of erosion events challenging. Nonetheless, the evidence from Tekkedere suggests that the transformation of large settlements (e.g., Pergamon and Elaia) from the Hellenistic Period to the Roman Imperial Period contributed to landscape change in rural areas, though the small catchment of Tekkedere reacted more sensitively to human activities than the higher-order catchment of the Bakırçay River. The ongoing pressure from local land use promotes the accumulation of the relatively young valley infills.

Acknowledgments. The research was carried out as part of the project “The Transformation of the Pergamon Micro-Region between the Hellenistic Period and the Roman Imperial Period” (<https://www.dainst.blog/transpergimikro>, accessed March 2022). The fieldwork was conducted as part of the Pergamon Excavation of the Istanbul Department of the German Archeological Institute (DAI), for which Felix Pirson holds the license. We would like to express our special thanks for the kind permission and support from the Ministry of Culture and Tourism of the Republic of Turkey and Ayşe Tok (Directorate Museum Demre) who took part in the works as a government representative. Murat Tozan and geography students from Ege University Izmir (Nami Yurtseven, Minel Korkmaz, and Elif Gültekin) and Freie Universität Berlin (Lena Schimmel) are acknowledged for their help during fieldwork and laboratory analyses. We also appreciate the help of colleagues from the DAI (Felix Pirson, Ulrich Mania, Paula Michalski, and Nicole Neuenfeld), Manisa Celal Bayar Üniversitesi (Güler Ateş), and the Bergama Museum. The authors declare that they have no known competing financial interests or personal relationships that could have appeared to influence the work reported in this paper.

Financial Support. We would like to acknowledge financial support from the China Scholarship Council (grant no. 201906190216) and Deutsche Forschungsgemeinschaft (German Research Foundation; grant number 419349690).

Supplementary Material. The supplementary material for this article can be found at <https://doi.org/10.1017/qua.2022.73>.

REFERENCES

- Ackermann, O., Greenbaum, N., Ayalon, A., Bar-Matthews, M., Boaretto, E., Bruins, H.J., Cabanes, D., et al., 2014. Using palaeo-environmental proxies to reconstruct natural and anthropogenic controls on sedimentation rates, Tell es-Safi/Gath, eastern Mediterranean. *Anthropocene* 8, 70–82.
- Aksu, A.E., Piper, D.J.W., Konuk, T., 1987. Late Quaternary tectonic and sedimentary history of outer Izmir and Candarli bays, western Turkey. *Marine Geology* 76, 89–104.
- Aucelli, P., Cinque, A., Mattei, G., Pappone, G., Stefanile, M., 2018. Coastal landscape evolution of Naples (southern Italy) since the Roman period from archaeological and geomorphological data at Palazzo degli Spiriti site. *Quaternary International* 483, 23–38.
- Avni, Y., Porat, N., Plakht, J., Avni, G., 2006. Geomorphic changes leading to natural desertification versus anthropogenic land conservation in an arid environment, the Negev Highlands, Israel. *Geomorphology* 82, 177–200.
- Bassukas, D., Emmanouilidis, A., Avramidis, P., 2021. Late Holocene hydroclimate variability in the eastern Mediterranean: a spatial multi-proxy approach. *Water* 13, 1–11.
- Becker, F., Knitter, D., Nykamp, M., Schütt, B., 2020a. Meta-Analysis of Geomorphodynamics in the Western Lower Bakırçay Plain (Aegean Region, Turkey). *Land* 9, 1–29.
- Becker, F., Knitter, D., Yang, X., Schütt, B., 2020b. Geländearbeiten der Physischen Geographie 2019. In: Pirson, F. (Ed.), *Pergamon—Das neue Forschungsprogramm und die Arbeiten in der Kampagne 2019*. *Archäologischer Anzeiger* 2, 223–227.
- Becker, F., Yang, X., Nykamp, M., Doğan, M., Schütt, B., 2022. Sedimentologische Arbeiten der Physischen Geographie. In: Pirson, F.

- (Ed.), *Pergamon—Die Arbeiten in der Kampagne 2020. Archäologischer Anzeiger* 2, 50–59.
- Bellin, N., Vanacker, V., De Baets, S.**, 2013. Anthropogenic and climatic impact on Holocene sediment dynamics in SE Spain: a review. *Quaternary International* 308–309, 112–129.
- Benito, G., Macklin, M.G., Zielhofer, C., Jones, A.F., Machado, M.J.**, 2015. Holocene flooding and climate change in the Mediterranean. *Catena* 130, 13–33.
- Bini, M., Zanchetta, G., Perşoiu, A., Cartier, R., Català, A., Cacho, I., Dean, J.R., et al.**, 2019. The 4.2 ka BP Event in the Mediterranean region: an overview. *Climate of the Past* 15, 555–577.
- Black, R., Adger, W.N., Arnell, N.W., Dercon, S., Geddes, A., Thomas, D.**, 2011. The effect of environmental change on human migration. *Global Environmental Change* 21, S3–S11.
- Blair, T.C., McPherson, J.G.**, 1994. Alluvial fans and their natural distinction from rivers based on morphology, hydraulic processes, sedimentary processes, and facies assemblages. *Journal of Sedimentary Research* 64, 450–489.
- Blair, T.C., McPherson, J.G.**, 1999. Grain-size and textural classification of coarse sedimentary particles. *Journal of Sedimentary Research* 69, 6–19.
- Blair, T.C., McPherson, J.G.**, 2009. Processes and forms of alluvial fans. In: Parsons, A.J., Abrahams, A.D. (Eds.), *Geomorphology of Desert Environments*. 2nd ed. Springer, Dordrecht, Netherlands, pp. 413–467.
- Blundell, A., Dearing, J.A., Boyle, J.F., Hannam, J.A.**, 2009. Controlling factors for the spatial variability of soil magnetic susceptibility across England and Wales. *Earth-Science Reviews* 95, 158–188.
- Bowman, D.**, 2019. *Principles of Alluvial Fan Morphology*. Springer, Dordrecht, Netherlands.
- Boyer, P., Roberts, N., Baird, D.**, 2006. Holocene environment and settlement on the Çarşamba alluvial fan, south-central Turkey: Integrating geoarchaeology and archaeological field survey. *Geoarchaeology* 21, 675–698.
- Bozkurt, E.**, 2003. Origin of NE-trending basins in western Turkey. *Geodinamica Acta* 16, 61–81.
- Bozyiğit, C., Eriş, K.K., Sicre, M.-A., Çağatay, M.N., Uçarkuş, G., Klein, V., Gasperini, L.**, 2022. Middle-late Holocene climate and hydrologic changes in the Gulf of Saros (NE Aegean Sea). *Marine Geology* 443, 1–13.
- Brisset, E., Miramont, C., Guiter, F., Anthony, E.J., Tachikawa, K., Poulenard, J., Arnaud, F., et al.**, 2013. Non-reversible geosystem destabilisation at 4200 cal. BP: Sedimentological, geochemical and botanical markers of soil erosion recorded in a Mediterranean alpine lake. *The Holocene* 23, 1863–1874.
- Brock, F., Higham, T., Ditchfield, P., Ramsey, C.B.**, 2010. Current pretreatment methods for AMS radiocarbon dating at the Oxford Radiocarbon Accelerator Unit (ORAU). *Radiocarbon* 52, 103–112.
- Bronk Ramsey, C.**, 2008. Radiocarbon dating: revolutions in understanding. *Archaeometry* 50, 249–275.
- Brown, A.G.**, 1997. *Alluvial Geoarchaeology: Floodplain Archaeology and Environmental Change*. Cambridge University Press, Cambridge.
- Brown, A.G., Walsh, K.**, 2017. Societal stability and environmental change: examining the archaeology-soil erosion paradox. *Geoarchaeology* 32, 23–35.
- Bulkan, Ö., Yalçın, M.N., Wilkes, H.**, 2018. Geochemistry of Marmara Lake sediments—implications for Holocene environmental changes in western Turkey. *Quaternary International* 486, 199–214.
- Butzer, K.W.**, 2005. Environmental history in the Mediterranean world: cross-disciplinary investigation of cause-and-effect for degradation and soil erosion. *Journal of Archaeological Science* 32, 1773–1800.
- Butzer, K.W.**, 2012. Collapse, environment, and society. *Proceedings of the National Academy of Sciences USA* 109, 3632–3639.
- Cartelle, V., García-Moreiras, I., Martínez-Carreño, N., Muñoz Sobrino, C., García-Gil, S.**, 2022. The role of antecedent morphology and changing sediment sources in the postglacial palaeogeographical evolution of an incised valley: the sedimentary record of the Ría de Arousa (NW Iberia). *Global and Planetary Change* 208, 1–21.
- Çelik, G., Karacakaya, R., Mete, Z., Genç, H., Bal, F.**, 2019. Disasters according to the Red Crescent archive documents, Ankara.
- Charlton, R.**, 2007. *Fundamentals of Fluvial Geomorphology*. Routledge, Oxford, UK.
- Chiverrell, R.C., Harvey, A.M., Foster, G.C.**, 2007. Hillslope gully in the Solway Firth—Morecambe Bay region, Great Britain: responses to human impact and/or climatic deterioration? *Geomorphology* 84, 317–343.
- Cole, B., Smith, G., Balzter, H.**, 2018. Acceleration and fragmentation of CORINE land cover changes in the United Kingdom from 2006–2012 detected by Copernicus IMAGE2012 satellite data. *International Journal of Applied Earth Observation and Geoinformation* 73, 107–122.
- Collins, P.E.F., Rust, D.J., Salih Bayraktutan, M., Turner, S.D.**, 2005. Fluvial stratigraphy and palaeoenvironments in the Pasinler Basin, eastern Turkey. *Quaternary International* 140–141, 121–134.
- Constante, A., Peña, J.L., Muñoz, A., Picazo, J.**, 2010. Climate and anthropogenic factors affecting alluvial fan development during the late Holocene in the central Ebro Valley, northeast Spain. *The Holocene* 21, 275–286.
- Crema, E.R., Bevan, A.**, 2021. Inference from large sets of radiocarbon dates: software and methods. *Radiocarbon* 63, 23–39.
- Danacıoğlu, S., Tağıl, Ş.**, 2017. Evaluation of the erosion risk by using the RUSLE model in Bakırçay basin. [In Turkish.] *Balikesir Üniversitesi Sosyal Bilimler Enstitüsü Dergisi* 20, 1–18.
- Dean, W.E.**, 1974. Determination of carbonate and organic matter in calcareous sediments and sedimentary rocks by loss on ignition; comparison with other methods. *Journal of Sedimentary Research* 44, 242–248.
- Dearing, J.A.**, 1994. *Environmental Magnetic Susceptibility: Using the Bartington MS2 System*. Chi Publishing, Kenilworth, UK.
- Dearing, J.A., Dann, R., Hay, K., Lees, J., Loveland, P., Maher, B.A., O’Grady, K.**, 1996. Frequency-dependent susceptibility measurements of environmental materials. *Geophysical Journal International* 124, 228–240.
- Dinelli, E., Tateo, F., Summa, V.**, 2007. Geochemical and mineralogical proxies for grain size in mudstones and siltstones from the Pleistocene and Holocene of the Po River alluvial plain, Italy. *Geological Society of America* 420, 25–36.
- Di Rita, F., Michelangeli, F., Celant, A., Magri, D.**, 2022. Sign-switching ecological changes in the Mediterranean Basin at 4.2 ka BP. *Global and Planetary Change* 208, 1–8.
- Doğan, T., İlkmén, E., Kulak, F.**, 2021. A new national 1 MV AMS laboratory at TÜBİTAK MRC in Turkey. *Nuclear Instruments and Methods in Physics Research Section B: Beam Interactions with Materials and Atoms* 509, 48–54.
- Dotterweich, M.**, 2008. The history of soil erosion and fluvial deposits in small catchments of central Europe: deciphering the long-term interaction between humans and the environment—a review. *Geomorphology* 101, 192–208.
- Dreibrodt, S., Lubos, C., Lomax, J., Sipos, G., Schroedter, T., Nelle, O.**, 2014. Holocene landscape dynamics at the tell Arslantepe, Malatya, Turkey—soil erosion, buried soils and settlement layers, slope and river activity in a middle Euphrates catchment. *The Holocene* 24, 1351–1368.
- Dusar, B., Verstraeten, G., D’Haen, K., Bakker, J., Kaptijn, E., Waelkens, M.**, 2012. Sensitivity of the Eastern Mediterranean geomorphic system towards environmental change during the Late Holocene: a chronological perspective. *Journal of Quaternary Science* 27, 371–382.
- Dusar, B., Verstraeten, G., Notebaert, B., Bakker, J.**, 2011. Holocene environmental change and its impact on sediment dynamics in the Eastern Mediterranean. *Earth-Science Reviews* 108, 137–157.
- Eastwood, W.J., Leng, M.J., Roberts, N., Davis, B.**, 2007. Holocene climate change in the eastern Mediterranean region: a comparison of stable isotope and pollen data from Lake Gölhisar, southwest Turkey. *Journal of Quaternary Science* 22, 327–341.
- Eastwood, W.J., Roberts, N., Lamb, H.F.**, 1998. Palaeoecological and archaeological evidence for human occupation in southwest Turkey: the Beyşehir Occupation Phase. *Anatolian Studies* 48, 69–86.
- Emre, Ö., Doğan, A., Özalp, S.**, 2011a. Active Fault Map Series of Turkey, Balıkesir (NJ 35-3) Quadrangle. Serial number: 4. 1:250,000. General Directorate of Mineral Research and Exploration, Ankara, Turkey.
- Emre, Ö., Özalp, S., Doğan, A., Özaksoy, V., Yildirim, C., Göktaş, F.**, 2005. İzmir yakın Çevresinin diri fayları ve deprem potansiyelleri [Active faults and earthquake potential in the İzmir region]. Maden tetkik ve arama genel müdürlüğü (Ed.), MTA Rapor No. 10754, 1–80. Jeoloji Etütleri Dairesi, İzmir, Turkey.
- Emre, Ö., Özalp, S., Duman, T.Y.**, 2011b. Active Fault Map Series of Turkey, İzmir (NJ 35-7) Quadrangle. Serial number: 6. 1:250,000. General Directorate of Mineral Research and Exploration, Ankara, Turkey.
- Fediuk, A., Wilken, D., Wunderlich, T., Rabbel, W., Seeliger, M., Laufer, E., Pirson, F.**, 2019. Marine seismic investigation of the ancient Kane harbour bay, Turkey. *Quaternary International* 511, 43–50.

- Feuser, S., Mania, U., Pirson, F., 2020. Stadtentwicklung und städtische Physiognomie im Kontext von Mikroregion oder Kulturlandschaft? Das Beispiel Elaia. In: Mohr, E.-M., Rheidt, K., Arslan, N. (Eds.), *Urbanism and Architecture in Ancient Aioli. (Proceedings of the International Conference from 7th–9th April 2017 in Çanakkale)*. Asia-Minor-Studien 95. Dr. Rudolf Habelt GmbH, Bonn, pp. 203–216.
- Finné, M., Holmgren, K., Sundqvist, H.S., Weiberg, E., Lindblom, M., 2011. Climate in the eastern Mediterranean, and adjacent regions, during the past 6000 years—a review. *Journal of Archaeological Science* **38**, 3153–3173.
- Finné, M., Woodbridge, J., Labuhn, I., Roberts, C.N., 2019. Holocene hydroclimatic variability in the Mediterranean: a synthetic multi-proxy reconstruction. *The Holocene* **29**, 847–863.
- Fowler, A.J., Gillespie, R., Hedges, R.E.M., 1986. Radiocarbon dating of sediments. *Radiocarbon* **28**, 441–450.
- Fryirs, K., 2013. (Dis)connectivity in catchment sediment cascades: a fresh look at the sediment delivery problem. *Earth Surface Processes and Landforms* **38**, 30–46.
- Fryirs, K.A., Brierley, G.J., Preston, N.J., Kasai, M., 2007. Buffers, barriers and blankets: the (dis)connectivity of catchment-scale sediment cascades. *Catena* **70**, 49–67.
- Fuchs, M., 2007. An assessment of human versus climatic impacts on Holocene soil erosion in NE Peloponnese, Greece. *Quaternary Research* **67**, 349–356.
- Gehrke, H.-J., 2014. A brief history of Pergamon. In: Scholl, A., Pirson, F. (Eds.), *Pergamon–Anadolu'da Hellenistik Bir Başkent/A Hellenistic Capital in Anatolia*. Yapi Kredi Yayinlari, Istanbul, pp. 122–141.
- Glais, A., Lespez, L., Vannière, B., López-Sáez, J.A., 2017. Human-shaped landscape history in NE Greece. A palaeoenvironmental perspective. *Journal of Archaeological Science: Reports* **15**, 405–422.
- Goldberg, P., Macphail, R.I., 2006. *Practical and Theoretical Geoarchaeology*. Blackwell, Malden, MA.
- Günther, G., Clemen, T., Duttmann, R., Schütt, B., Knitter, D., 2021. Of animal husbandry and food production—a first step towards a modular agent-based modelling platform for socio-ecological dynamics. *Land* **10**, 1–25.
- Heiri, O., Lotter, A.F., Lemcke, G., 2001. Loss on ignition as a method for estimating organic and carbonate content in sediments: reproducibility and comparability of results. *Journal of Paleolimnology* **25**, 101–110.
- Horejs, B., 2010b. Yeni Yeldeğirmentepe. In: Pirson, F. (Ed.), *Pergamon—Bericht über die Arbeiten in der Kampagne 2009*. *Archäologischer Anzeiger* **2**, 164–168.
- Horejs, B., 2011b. Prähistorische Surveys am Yeni Yeldeğirmentepe und im Umland von Pergamon. In: Pirson, F. (Ed.), *Pergamon—Bericht über die Arbeiten in der Kampagne 2010*. *Archäologischer Anzeiger* **2**, 146–150.
- Horejs, B., 2014. Pergamon and the Kaikos Valley in prehistoric times. In: Scholl, A., Pirson, F. (Eds.), *Pergamon–Anadolu'da Hellenistik Bir Başkent/A Hellenistic Capital in Anatolia*. Yapi Kredi Yayinlari, Istanbul, pp. 106–119.
- Horejs, B., 2010a. Bronzezeitliche Besiedlungsmuster im Kaikostal. Interpretationen erster Surveyergebnisse im Umland von Pergamon (Türkei). In: Horejs, B., Kienlin, T.L. (Eds.), *Siedlung und Handwerk—Studien zu sozialen Kontexten in der Bronzezeit*. Dr. Rudolf Habelt, Bonn, Germany, pp. 47–67.
- Horejs, B., 2011a. Bergama and the Bakırçay Valley in Prehistory. In: Önen, E., Mutluer, M., Çetin, N. (Eds.), *International Bergama Symposium, Bergama, Turkey*, April 7–9, 2011, pp. 48–65.
- Jahn, R., Blume, H.-P., Asio, V.B., Spaargaren, O., Schad, P., 2006. *Guidelines for Soil Description*. 4th ed. FAO, Rome.
- Jalut, G., Dedoubat, J.J., Fontugne, M., Otto, T., 2009. Holocene circum-Mediterranean vegetation changes: climate forcing and human impact. *Quaternary International* **200**, 4–18.
- Jouffroy-Bapicot, I., Pedrotta, T., Debet, M., Field, S., Sulpizio, R., Zanchetta, G., Sabatier, P., et al., 2021. Olive groves around the lake. A ten-thousand-year history of a Cretan landscape (Greece) reveals the dominant role of humans in making this Mediterranean ecosystem. *Quaternary Science Reviews* **267**, 1–24.
- Kaniewski, D., Paulissen, E., De Laet, V., Dossche, K., Waelkens, M., 2007. A high-resolution Late Holocene landscape ecological history inferred from an intramontane basin in the Western Taurus Mountains, Turkey. *Quaternary Science Reviews* **26**, 2201–2218.
- Kapur, S., Akça, E., Günal, H., 2017. *The Soils of Turkey*. Springer, Cham, Switzerland.
- Kayan, İ., 1999. Holocene stratigraphy and geomorphological evolution of the Aegean coastal plains of Anatolia. *Quaternary Science Reviews* **18**, 541–548.
- Kayan, İ., Vardar, S., 2007. The physical geography of the Madra River Delta. In: Lambrianides, K., Spencer, N. (Eds.), *The Madra River Delta: Regional Studies on the Aegean Coast of Turkey 1: Environment, Society and Community from Prehistory to the Present*. British Institute at Ankara, London, pp. 9–23.
- Kennett, D.J., Masson, M., Lope, C.P., Serafin, S., George, R.J., Spencer, T.C., Hoggarth, J.A., et al., 2022. Drought-induced civil conflict among the ancient Maya. *Nature Communications* **13**, 1–10.
- Kidder, T.R., Adelsberger, K.A., Arco, L.J., Schilling, T.M., 2008. Basin-scale reconstruction of the geological context of human settlement: an example from the lower Mississippi Valley, USA. *Quaternary Science Reviews* **27**, 1255–1270.
- Knipping, M., Müllenhoff, M., Brückner, H., 2007. Human induced landscape changes around Bafa Gölü (western Turkey). *Vegetation History and Archaeobotany* **17**, 365–380.
- Knitter, D., 2013. *Central Places and the Environment: Investigations of an Interdependent Relationship*. Department of Earth Sciences, Freie Universität Berlin, Berlin, pp. 59–65.
- Kobes, v.J., 1999. *Fremdes Getreide. Beobachtungen zum Problem der Getreideversorgung in der kaiserzeitlichen Provinz Asia, Laverna: Beiträge zur Wirtschafts- und Sozialgeschichte der Alten Welt*. Scripta Mercaturae-Verlag, St. Katharinen, Germany, pp. 81–98.
- Kondolf, M., Piégay, H., 2011. Geomorphology and society. In: Gregory, K.J., Goudie, A.S. (Eds.), *The SAGE Handbook of Geomorphology*. Sage, London, pp. 105–118.
- Kovda, I., Lynn, W., Williams, D., Chichagova, O., 2001. Radiocarbon age of vertisols and its interpretation using data on Gilgai Complex in the North Caucasus. *Radiocarbon* **43**, 603–610.
- Kuzucuoglu, C., Dörfler, W., Kunesch, S., Goupille, F., 2011. Mid- to late-Holocene climate change in central Turkey: the Tecer Lake record. *The Holocene* **21**, 173–188.
- Laabs, J., Knitter, D., 2021. How much is enough? First steps to a social ecology of the Pergamon microregion. *Land* **10**, 1–19.
- Lang, A., Hönscheidt, S., 1999. Age and source of colluvial sediments at Vaihingen—Enz, Germany. *Catena* **38**, 89–107.
- Lawrence, D., Palmisano, A., de Gruchy, M.W., 2021. Collapse and continuity: a multi-proxy reconstruction of settlement organization and population trajectories in the northern Fertile Crescent during the 4.2kya rapid climate change event. *PLoS ONE* **16**, 1–20.
- Ludwig, B., 2020b. Reconstructing the ancient route network in Pergamon's surroundings. *Land* **9**, 1–39.
- Ludwig, B., 2019. Das Umland von Pergamon. Die Arbeiten des Umland-Surveys 2018. In: Pirson, F. (Ed.), *Pergamon—Bericht über die Arbeiten in der Kampagne 2018*. *Archäologischer Anzeiger* **2**, 113–116.
- Ludwig, B., 2020a. Das Umland von Pergamon. Die Arbeiten des Umland-Surveys 2019. In: Pirson, F. (Ed.), *Pergamon—Das neue Forschungsprogramm und die Arbeiten in der Kampagne 2019*. *Archäologischer Anzeiger* **2**, 205–216.
- Lü, J., Mo, D., Zhuang, Y., Jiang, J., Liao, Y., Lu, P., Ren, X., Feng, J., 2019. Holocene geomorphic evolution and settlement distribution patterns in the mid-lower Fen River basins, China. *Quaternary International* **521**, 16–24.
- Lynch, J., 1990. Provisional elemental values for eight new geochemical lake sediment and stream sediment reference materials LKSD-1, LKSD-2, LKSD-3, LKSD-4, STSD-1, STSD-2, STSD-3, and STSD-4*. *Geostandards Newsletter* **14**, 153–167.
- Macphail, R.I., Goldberg, P., 2017. *Applied Soils and Micromorphology in Archaeology*. Cambridge University Press, Cambridge.
- Maher, B.A., Thompson, R., 1991. Mineral magnetic record of the Chinese loess and paleosols. *Geology* **19**, 3–6.
- May, S.M., Norpoth, M., Pint, A., Shumilovskikh, L., Raith, K., Brill, D., Rixhon, G., et al., 2021. Mid- to late Holocene environmental changes and human-environment interactions in the surroundings of La Silla del Papa, SW Spain. *Geoarchaeology* **36**, 573–600.

- McHugh, C.M.G., Seeber, L., Cormier, M.-H., Dutton, J., Cagatay, N., Polonia, A., Ryan, W.B.F., Gorur, N., 2006. Submarine earthquake geology along the North Anatolia Fault in the Marmara Sea, Turkey: a model for transform basin sedimentation. *Earth and Planetary Science Letters* **248**, 661–684.
- McLeman, R.A., 2011. Settlement abandonment in the context of global environmental change. *Global Environmental Change* **21**, S108–S120.
- Mecking, R., Meinecke, M., Erkul, E., Driehaus, B., Bolten, A., Pirson, F., Rabbel, W., 2020. The Yığma Tepe of Pergamon: stratigraphic construction of a monumental tumulus from seismic refraction measurements. *Archaeological Prospection* **27**, 73–105.
- Miall, A., 2014. *Fluvial Depositional Systems*. Springer International, Cham, Switzerland.
- Miall, A.D., 2006. *The Geology of Fluvial Deposits: Sedimentary Facies, Basin Analysis, and Petroleum Geology*. Springer, Berlin, Germany.
- Michalski, P., 2021. *A Rural Settlement in the Surroundings of Pergamon—Survey Analysis of the Kuyulu Kaya in the Lower Western Kaikos Valley*. Humboldt-Universität zu Berlin, Berlin, pp. 1–292.
- Mills, H.H., 1979. Downstream rounding of pebbles—a quantitative review. *Journal of Sedimentary Research* **49**, 295–302.
- [MTA] Maden tetkik ve arama genel müdürlüğü [General Directorate of Mineral Research and Exploration], 2002. Geological Map of Turkey (İzmir). 1:500,000. General Directorate of Mineral Research and Exploration, Ankara, Turkey.
- Nalbant, S.S., Hubert, A., King, G.C.P., 1998. Stress coupling between earthquakes in northwest Turkey and the north Aegean Sea. *Journal of Geophysical Research: Solid Earth* **103**, 24469–24486.
- Nykamp, M., Becker, F., Braun, R., Pöllath, N., Knitter, D., Peters, J., Schütt, B., 2021. Sediment cascades and the entangled relationship between human impact and natural dynamics at the pre-pottery Neolithic site of Göbekli Tepe, Anatolia. *Earth Surface Processes and Landforms* **46**, 430–442.
- Nykamp, M., Knitter, D., Schütt, B., 2020. Late Holocene geomorphodynamics in the vicinity of Göbekli Tepe, SE Turkey. *Catena* **195**, 1–14.
- Ocakoglu, F., Çilingiroglu, Ç., Erkara, İ.P., Ünan, S., Dinçer, B., Akkiraz, M.S., 2019. Human-climate interactions since the neolithic period in Central Anatolia: novel multi-proxy data from the Kureysler area, Kütahya, Turkey. *Quaternary Science Reviews* **213**, 1–17.
- Özpolat, E., Yıldırım, C., Görüm, T., 2020. The Quaternary landforms of the Büyük Menderes Graben System: the southern Menderes Massif, western Anatolia, Turkey. *Journal of Maps* **16**, 405–419.
- Özpolat, E., Yıldırım, C., Görüm, T., Gosse, J.C., Şahiner, E., Şarıkaya, M.A., Owen, L.A., 2022. Three-dimensional control of alluvial fans by rock uplift in an extensional regime: Aydın Range, Aegean extensional province. *Scientific Reports* **12**, 1–14.
- Palmisano, A., Lawrence, D., de Gruchy, M.W., Bevan, A., Shennan, S., 2021. Holocene regional population dynamics and climatic trends in the Near East: a first comparison using archaeo-demographic proxies. *Quaternary Science Reviews* **252**, 1–27.
- Panin, P.G., Filippova, K.G., Bukhonov, A.V., Karpukhina, N.V., Kalinin, P.I., Ruchkin, M.V., 2021. High-resolution analysis of the Likhvin loess-paleosol sequence (the central part of the East European Plain, Russia). *Catena* **205**, 1–15.
- Paradisopoulou, P.M., Papadimitriou, E.E., Karakostas, V.G., Taymaz, T., Kilias, A., Yolsal, S., 2010. Seismic hazard evaluation in western Turkey as revealed by stress transfer and time-dependent probability calculations. *Pure and Applied Geophysics* **167**, 1013–1048.
- Pavúk, P., Horejs, B., 2018. Ceramics, surveys, and connectivity in western Anatolia: the Middle and Late Bronze Age Bakırçay/Kaikos Valley restudied. *Ägypten Levante* **28**, 457–485.
- Peel, M.C., Finlayson, B.L., McMahon, T.A., 2007. Updated world map of the Köppen-Geiger climate classification. *Hydrology and Earth System Sciences* **11**, 1633–1644.
- Pérez-Lambán, F., Peña-Monné, J.L., Badía-Villas, D., Picazo Millán, J.V., Sampietro-Vattuone, M.M., Alcolea Gracia, M., Aranbarri, J., González-Sampériz, P., Fanlo Loras, J., 2018. Holocene environmental variability in the Central Ebro Basin (NE Spain) from geoarchaeological and pedological records. *Catena* **163**, 147–164.
- Pint, A., Seeliger, M., Frenzel, P., Feuser, S., Erkul, E., Berndt, C., Klein, C., Pirson, F., Brückner, H., 2015. The environs of Elaiia's ancient open harbour—a reconstruction based on microfaunal evidence. *Journal of Archaeological Science* **54**, 340–355.
- Pirson, F., 2017. Die Siedlungsgeschichte Pergamons. Überblick und kritische Revision. Mit einem Appendix von Anneke Keweloh-Kaletta. *Istanbuler Mitteilungen* **67**, 43–130.
- Pirson, F., 2020. Pergamon—Das neue Forschungsprogramm und die Arbeiten in der Kampagne 2019. *Archäologischer Anzeiger* **2**, 1–245.
- Pirson, F., 2022. Pergamon—Die Arbeiten in der Kampagne 2020. *Archäologischer Anzeiger* **2**, 1–95.
- Pirson, F., 2008. Das Territorium der hellenistischen Residenzstadt Pergamon: Herrschaftlicher Anspruch als raumbezogene Strategie. In: Jöchner, C. (Ed.), *Räume der Stadt: Von der Antike bis heute*. Reimer, Berlin, pp. 27–50.
- Pirson, F., 2014. Elaiia, der (maritime) Satellit Pergamons. In: Ladstätter, S., Pirson, F., Schmidts, T. (Eds.), *Harbors and Harbor Cities in the Eastern Mediterranean from Antiquity to the Byzantine Period: Recent Discoveries and Current Approaches*. Byzas, Istanbul, pp. 339–356.
- Pirson, F., Ateş, G., Bartz, M., Brückner, H., Feuser, S., Mania, U., Meier, L., Seeliger, M., 2015. Elaiia: Eine aiolische Polis im Dienste der hellenistischen Residenzstadt Pergamon? In: Matthaei, A., Zimmermann, M. (Eds.), *Urbane Strukturen und bürgerliche Identität im Hellenismus*. Verlag Antike, Heidelberg, Germany, pp. 22–55.
- Pirson, F., Zimmermann, M., 2014. The hinterland of Pergamon. Economic resources, rural settlements and political manifestation. In: Scholl, A., Pirson, F. (Eds.), *Pergamon—Anadolu'da Hellenistik Bir Başkent / A Hellenistic Capital in Anatolia*. Yapi Kredi Yayinlari, Istanbul, pp. 144–161.
- R Core Team, 2021. *R: A Language and Environment for Statistical Computing*. R Foundation for Statistical Computing, Vienna.
- Reimer, P.J., Austin, W.E.N., Bard, E., Bayliss, A., Blackwell, P.G., Bronk Ramsey, C., Butzin, M., et al., 2020. The IntCal20 Northern Hemisphere Radiocarbon Age Calibration Curve (0–55 cal kBP). *Radiocarbon* **62**, 725–757.
- Remondo, J., Soto, J., González-Díez, A., Díaz de Terán, J.R., Cendrero, A., 2005. Human impact on geomorphic processes and hazards in mountain areas in northern Spain. *Geomorphology* **66**, 69–84.
- Roberts, C.N., Woodbridge, J., Palmisano, A., Bevan, A., Fyfe, R., Shennan, S., 2019a. Mediterranean landscape change during the Holocene: synthesis, comparison and regional trends in population, land cover and climate. *The Holocene* **29**, 923–937.
- Roberts, N., 2019. How humans changed the face of Earth. *Science* **365**, 865–866.
- Roberts, N., Allcock, S.L., Barnett, H., Mather, A., Eastwood, W.J., Jones, M., Primmer, N., Yiğitbaşoğlu, H., Vannière, B., 2019b. Cause-and-effect in Mediterranean erosion: the role of humans and climate upon Holocene sediment flux into a central Anatolian lake catchment. *Geomorphology* **331**, 36–48.
- Roberts, N., Brayshaw, D., Kuzucuoğlu, C., Perez, R., Sadori, L., 2011. The mid-Holocene climatic transition in the Mediterranean: causes and consequences. *The Holocene* **21**, 3–13.
- Robustelli, G., Lucà, F., Corbi, F., Pelle, T., Dramis, F., Fubelli, G., Scarciglia, F., Muto, F., Cugliari, D., 2009. Alluvial terraces on the Ionian coast of northern Calabria, southern Italy: implications for tectonic and sea level controls. *Geomorphology* **106**, 165–179.
- Santisteban, J.I., Mediavilla, R., López-Pamo, E., Dabrio, C.J., Zapata, M.B.R., García, M.J.G., Castaño, S., Martínez-Alfaro, P.E., 2004. Loss on ignition: a qualitative or quantitative method for organic matter and carbonate mineral content in sediments? *Journal of Paleolimnology* **32**, 287–299.
- Sauer, T., Ries, J.B., 2008. Vegetation cover and geomorphodynamics on abandoned fields in the Central Ebro Basin (Spain). *Geomorphology* **102**, 267–277.
- Scharpenseel, H., Schiffmann, H., 1977. Soil radiocarbon analysis and soil dating. *Geophysical Surveys* **3**, 143–156.
- Schneider, S., Matthaei, A., Bebermeier, W., Schütt, B., 2014. Late Holocene human–environmental interactions in the eastern Mediterranean: settlement history and paleogeography of an ancient Aegean hill-top settlement. *Quaternary International* **324**, 84–98.

- Schneider, S., Matthaei, A., Schlöffel, M., Meyer, C., Kronwald, M., Pint, A., Schütt, B., 2015. A geoarchaeological case study in the chora of Pergamon, western Turkey, to reconstruct the late Holocene landscape development and settlement history. *Quaternary International* **367**, 62–76.
- Schneider, S., Nykamp, M., Matthaei, A., Bebermeier, W., Schütt, B., 2013. Alluvial geoarchaeology of a small drainage basin in western Anatolia: Late Holocene landscape development and the question of the mouth of the paleo-Bakırçay. *Quaternary International* **312**, 84–95.
- Schneider, S., Schlöffel, M., Schwall, C., Horejs, B., Schütt, B., 2017. First stratigraphic evidence and absolute dating of a Bronze Age settlement in the Bakırçay valley in western Turkey. *Journal of Archaeological Science: Reports* **12**, 316–322.
- Shumm, S.A., 1977. *The Fluvial System*. Wiley, New York.
- Seeliger, M., Bartz, M., Erkul, E., Feuser, S., Kelterbaum, D., Klein, C., Pirson, F., Vött, A., Brückner, H., 2013. Taken from the sea, reclaimed by the sea: the fate of the closed harbour of Elaia, the maritime satellite city of Pergamon (Turkey). *Quaternary International* **312**, 70–83.
- Seeliger, M., Brill, D., Feuser, S., Bartz, M., Erkul, E., Kelterbaum, D., Vött, A., Klein, C., Pirson, F., Brückner, H., 2014. The purpose and age of underwater walls in the Bay of Elaia of western Turkey: a multidisciplinary approach. *Geoarchaeology* **29**, 138–155.
- Seeliger, M., Pint, A., Feuser, S., Riedesel, S., Marriner, N., Frenzel, P., Pirson, F., Bolten, A., Brückner, H., 2019. Elaia, Pergamon's maritime satellite: the rise and fall of an ancient harbour city shaped by shoreline migration. *Journal of Quaternary Science* **34**, 228–244.
- Seeliger, M., Pint, A., Frenzel, P., Feuser, S., Pirson, F., Riedesel, S., Brückner, H., 2017. Foraminifera as markers of Holocene sea-level fluctuations and water depths of ancient harbours—a case study from the Bay of Elaia (W Turkey). *Palaeogeography, Palaeoclimatology, Palaeoecology* **482**, 17–29.
- Sherriff, S.C., 2014. Environmental magnetism: sediment source tracing. In: Cook, S.J., Clarke, L.E., Nield, J.M. (Eds.), *Geomorphological Techniques (Online Edition)*. British Society for Geomorphology, London, pp. 1–14.
- Shumilovskikh, L.S., Seeliger, M., Feuser, S., Novenko, E., Schlütz, F., Pint, A., Pirson, F., Brückner, H., 2016. The harbour of Elaia: a palynological archive for human environmental interactions during the last 7500 years. *Quaternary Science Reviews* **149**, 167–187.
- Soil Science Division Staff, 2017. *Soil Survey Manual*. 4th ed. Handbook No. 18. USDA, Washington, DC.
- Soil Survey Staff, 1999. *Soil Taxonomy: A Basic System of Soil Classification for Making and Interpreting Soil Surveys*. 2nd ed. USDA, Washington, DC.
- Sommerey, K.M., 2008. Die Chora von Pergamon: Studien zu Grenzen, Siedlungsstruktur und Wirtschaft. In: Pirson, F., Bachmann, M. (Eds.), *Istanbul Mitteilungen*. Ernst Wasmuth, Tübingen, Germany, pp. 135–170.
- Stock, F., Laermanns, H., Pint, A., Knipping, M., Wulf, S., Hassl, A.R., Heiss, A.G., et al., 2020. Human-environment interaction in the hinterland of Ephesos—as deduced from an in-depth study of Lake Belevi, west Anatolia. *Quaternary Science Reviews* **244**, 1–17.
- Stow, D.A., 2005. *Sedimentary Rocks in the Field: A Color Guide*. Manson Publishing, London.
- Strunk, A., Olsen, J., Sanei, H., Rudra, A., Larsen, N.K., 2020. Improving the reliability of bulk sediment radiocarbon dating. *Quaternary Science Reviews* **242**, 1–13.
- Terry, R.E., 2017. Field geochemistry. In: Gilbert, A.S. (Ed.), *Encyclopedia of Geoarchaeology*. Springer Reference, Dordrecht, pp. 263–271.
- Tozan, M., 2022. Osmanische Dokumente und ihre Bedeutung für die historischarchäologische Erforschung der Mikroregion Pergamon: Perspektiven und erste Beobachtungen. In: Pirson, F. (Ed.), *Pergamon—Die Arbeiten in der Kampagne 2020*. *Archäologischer Anzeiger* **2**, 47–49.
- Türkeş, M., Erlat, E., 2005. Climatological responses of winter precipitation in Turkey to variability of the North Atlantic Oscillation during the period 1930–2001. *Theoretical and Applied Climatology* **81**, 45–69.
- Ülgen, U.B., Franz, S.O., Biltekin, D., Çagatay, M.N., Roeser, P.A., Doner, L., Thein, J., 2012. Climatic and environmental evolution of Lake Iznik (NW Turkey) over the last ~4700 years. *Quaternary International* **274**, 88–101.
- van Andel, T.H., Zangger, E., Demitrack, A., 1990. Land use and soil erosion in prehistoric and historical Greece. *Journal of Field Archaeology* **17**, 379–396.
- Verstraeten, G., Broothaerts, N., Van Loo, M., Notebaert, B., D'Haen, K., Duser, B., De Brue, H., 2017. Variability in fluvial geomorphic response to anthropogenic disturbance. *Geomorphology* **294**, 20–39.
- Vita-Finzi, C., 1969. *The Mediterranean Valleys: Geological Changes in Historical Times*. Cambridge University Press, Cambridge.
- Vött, A., Brückner, H., Handl, M., Schriever, A., 2006. Holocene palaeogeographies of the Astakos coastal plain (Akarnania, NW Greece). *Palaeogeography, Palaeoclimatology, Palaeoecology* **239**, 126–146.
- Walker, M., Head, M.J., Lowe, J., Berkelhammer, M., Björck, S., Cheng, H., Cwynar, L.C., et al., 2019. Subdividing the Holocene Series/Epoch: formalization of stages/ages and subseries/subepochs, and designation of GSSPs and auxiliary stratotypes. *Journal of Quaternary Science* **34**, 173–186.
- Walsh, K., Berger, J.-F., Roberts, C.N., Vanniere, B., Ghilardi, M., Brown, A.G., Woodbridge, J., et al., 2019. Holocene demographic fluctuations, climate and erosion in the Mediterranean: a meta data-analysis. *The Holocene* **29**, 864–885.
- Wang, Y., Amundson, R., Trumbore, S., 1996. Radiocarbon dating of soil organic matter. *Quaternary Research* **45**, 282–288.
- Weiberg, E., Bonnier, A., Finné, M., 2021. Land use, climate change and “boom-bust” sequences in agricultural landscapes: interdisciplinary perspectives from the Peloponnese (Greece). *Journal of Anthropological Archaeology* **63**, 1–12.
- Weiberg, E., Hughes, R.E., Finné, M., Bonnier, A., Kaplan, J.O., 2019. Mediterranean land use systems from prehistory to antiquity: a case study from Peloponnese (Greece). *Journal of Land Use Science* **14**, 1–20.
- Weiss, H., 2016. Global megadrought, societal collapse and resilience at 4.2–3.9 ka BP across the Mediterranean and west Asia. *PAGES Magazine* **24**, 62–63.
- Wessel, B., Huber, M., Wohlfart, C., Marschalk, U., Kosmann, D., Roth, A., 2018. Accuracy assessment of the global TanDEM-X Digital Elevation Model with GPS data. *ISPRS Journal of Photogrammetry and Remote Sensing* **139**, 171–182.
- Williamson, C.G., 2016. Mountain, myth, and territory: Teuthrania as focal point in the landscape of Pergamon. In: McNerney, J., Sluiter, I. (Eds.), *Valuing Landscape in Classical Antiquity: Natural Environment and Cultural Imagination*. Brill, Leiden, pp. 70–99.
- Wulf, U., 1994. Der Stadtplan von Pergamon: zu Entwicklung und Stadtstruktur von der Neugründung unter Philetairos bis in spätantike Zeit. *Istanbul Mitteilungen* **44**, 135–175.
- Yang, X., Becker, F., Knitter, D., Schütt, B., 2021. An overview of the geomorphological characteristics of the Pergamon micro-region (Bakırçay and Madra River Catchments, Aegean Region, west Turkey). *Land* **10**, 1–27.
- Yang, X., Becker, F., Nykamp, M., Schütt, B., 2022. Dataset of sediment analyses (pH, electrical conductivity, magnetic susceptibility, loss on ignition, and X-ray fluorescence) from the Tekkedere catchment in the Pergamon micro-region, western Turkey (accessed January 4, 2023). <https://doi.org/10.1594/PANGAEA.944177>.
- Yilmaz, Y., Genç, Ş.C., Gürer, F., Bozcu, M., Yilmaz, K., Karacik, Z., Altunkaynak, Ş., Elmas, A., 2000. When did the western Anatolian grabens begin to develop?. In: Bozkurt, E., Winchester, J.A., Piper, J.D.A. (Eds.), *Tectonics and Magmatism in Turkey and the Surrounding Area*. Geological Society of London, London, pp. 353–384.
- Zhang, H., Cheng, H., Sinha, A., Spötl, C., Cai, Y., Liu, B., Kathayat, G., et al., 2021. Collapse of the Liangzhu and other Neolithic cultures in the lower Yangtze region in response to climate change. *Science Advances* **7**, 1–9.
- Zimmermann, M., 2011. *Pergamon. Geschichte, Kultur, Archäologie*. C.H. Beck, Munich.
- Zimmermann, M., Matthaei, A., Ateş, G., 2015. Die Chora von Pergamon: Forschungen im Kaikostal und in der antiken Stadt Atarneus. In: Matthaei, A., Zimmermann, M. (Eds.), *Urbane Strukturen und bürgerliche Identität im Hellenismus*. Verlag Antike, Heidelberg, Germany, pp. 193–236.